Energy Conversion and Management 349 (2026) 120842

Contents lists available at ScienceDirect

Energy Conversion and Management

journal homepage: www.elsevier.com/locate/enconman

Research Paper

Towards predictive multidimensional modeling for industrializing microwave air plasma-based NO_x formation

Matthias Albrechts *, Ivan Tsonev, Vojtěch Laitl, Annemie Bogaerts

Research Group PLASMANT and Center of Excellence PLASMA, Department of Chemistry, University of Antwerp, Belgium
Electrification Institute, University of Antwerp, Olieweg 97, 2020 Antwerp, Belgium

ARTICLE INFO

Keywords:
Nitrogen fixation
Microwave plasma
Computational fluid dynamics
Multiphysics modeling

ABSTRACT

We present a fluid model for (near-)atmospheric pressure air microwave plasma that couples fluid dynamics, microwave field heating, thermal chemistry, and the transport of chemically reactive species. The model is validated against experimental data from [1], which investigated an open microwave torch for NO_x formation from air at 0.65 bar and specific energy inputs below 52 kJ/mol. The laminar model accurately reproduces the temperature profile, while both the laminar and turbulent models show excellent agreement with experimental results for NO_x production. Additional validation is performed using the experimental results of [2] at atmospheric pressure, encompassing a broad range of flow rates (5–90 slm) and specific energy inputs (10–300 kJ/mol). For both laminar and turbulent flow, the model demonstrates good agreement with experimental measurements of core electron densities and NO_x concentrations at the outlet. Furthermore, analysis of the simulation results provides detailed insights into the mechanisms of NO_x formation and quenching within the plasma and its effluent. These insights highlight the benefits of high operating pressures and, for specific energy inputs above 100 kJ/mol, the need for rapid quenching beyond passive wall cooling. As the model does not rely on experimental data for parameterization, it offers predictive capabilities that make it a valuable tool for model-driven plasma reactor design.

1. Introduction

While the Haber-Bosch (H-B) process remains the dominant method for industrial nitrogen fixation (NF), it is associated with significant environmental challenges. The process accounts for approximately 1–2 % of global energy consumption and 2 % of natural gas usage, contributing to the release of 300 million metric tons of CO_2 annually [3]. Moreover, the H-B process is not cost-efficient at small scale and industrial plants typically produce a minimum of 100 tons of ammonia (NH_3) per day [4], increasing transport costs. Additionally, the operation of the H-B process requires high temperatures (350–500 °C) and high pressures (100–300 bar), which makes it difficult to adapt to varying loads arising from intermittent renewable energy sources [5].

Plasma processes offer several advantages, including the use of abundant resources such as air and water, operation via electricity, and flexible, scalable setups with rapid on/off capability, making them well-suited for integration with renewable energy sources [6,7]. Consequently, various plasma types and reactor designs have been explored for NF in the context of fertilizer production, and especially NO_x production from air is promising (rather than NH_3 synthesis) [5,8]. While non-thermal plasmas can theoretically achieve superior energy efficiency (an energy cost (EC) of 0.2 MJ/mol was postulated in [9]) compared to warm plasmas (theoretical EC of 0.86 MJ/mol under conditions of 20–30 bar [9]), experimental data often report much higher EC for cold plasmas, e.g. 5–100 MJ/mol [5,10–12]. Although the best results, i.e., 0.84 MJ/mol with 6 % NO concentration (50 Torr) [13] and 0.28 MJ/mol with 14 % NO concentration [14], were achieved in low-pressure microwave plasmas, these spectacular results achieved in the 1980 s have not been reproduced and warrant critical assessment. Furthermore, the reported low EC values account only for plasma power and exclude the energy demands of vacuum equipment and reactor cooling systems.

Warm plasmas, such as gliding arcs (GA), atmospheric pressure glow discharges (APGD) and microwave (MW) plasmas, have been extensively investigated for their potential in gas conversion applications. Vervloessem et al. [15] studied NO_x formation in a reverse-vortex flow GA, achieving a NO_x yield of 1.5 % with an EC of 3.6 MJ/mol for a 70/30 feed ratio of N_2/O_2. Li et al. [16] recently demonstrated a 40 %

* Corresponding author.
E-mail address: matthias.albrechts@uantwerpen.be (M. Albrechts).

https://doi.org/10.1016/j.enconman.2025.120842
Received 11 September 2025; Received in revised form 16 November 2025; Accepted 26 November 2025
Available online 9 December 2025

reduction in EC in their glow discharge system by lowering the cathode-fall voltage through the use of iron electrodes, achieving an EC of 3.7 MJ/mol. Pei et al. [17] reported a 45 % drop in EC by introducing an Al_2O_3 catalyst downstream of their DC glow discharge, reaching an EC of 2.9 MJ/mol. Jardali et al. [18] used a rotating GA (RGA) and reported a NO_x yield up to 5.5 % for an EC of 2.5 MJ/mol at an N_2/O_2 ratio of 50/50, and these values were further improved by combining the RGA with a so-called effusion nozzle (for post-plasma quenching) to a NO_x yield up to 5.9 % for an EC of 2.1 MJ/mol [19]. Likewise, Tsonev et al. [20] applied the above RGA under elevated pressures (up to 3 barg), reporting a record-low EC of 1.8 MJ/mol (N_2/O_2 ratio of 50/50) alongside a high production rate of 69 g/h and remarkable NO_2 selectivity (94 %), important for HNO_3 (and fertilizer) production. Recent research by Abdelaziz et al. [21] demonstrated an EC of 2.1 MJ/mol at relatively high flow rates of 4 L/min using a high-frequency spark discharge, again at an N_2/O_2 ratio of 50/50.

In recent years, microwave power sources have gained significant traction in plasma generation due to their precise control and operational stability [22,23]. Unlike (gliding) arc plasmas, they eliminate the need for electrode equipment, thereby preventing electrode erosion, which can otherwise compromise operational longevity [24]. Kelly et al. [25] highlighted the potential of atmospheric pressure air microwave plasma-based NO_x formation, achieving an EC of 2 MJ/mol for a total NO_x production of 3.8 % (N_2/O_2 ratio of 50/50), which is among the most efficient ECs reported in the literature.

Despite the various advantages of MW plasma and their relatively low EC (as well as of other warm plasmas, like gliding arc and glow discharge) for NF compared to other plasma sources, it remains too energy-intensive to compete with the H-B + Ostwald process. Indeed, a recent techno-economic analysis revealed that plasma-based NF would need to achieve an EC of 1–1.5 MJ/mol to become fully competitive with the H-B + Ostwald process [26]. Tsonev et al. [27] calculated the thermodynamic equilibrium limit for NO production in atmospheric pressure air plasmas as 4.5 % NO with EC of 2.7 MJ/mol. However, this combination of relatively high NO concentration and low EC has not yet been achieved experimentally, as the values reported above were for equimolar N_2/O_2 fractions [15,18–21,25], which always exhibit lower EC. Consequently, there is a critical need to develop more efficient plasma reactor designs, to further improve their performance, and to reach this target EC.

In order to improve current plasma reactor designs, a comprehensive understanding of the physical and chemical mechanisms governing reactor performance is essential. Zero-dimensional (0D) models serve as valuable tools for elucidating chemical processes due to their ability to incorporate extensive chemical kinetic schemes with minimal computational cost [28,29]. Numerous kinetic schemes for air plasma have been developed in the literature, providing insights into the intricate interplay between electronically and vibrationally excited states of N_2, N, O_2, O, and NO [30–32]. Given the large number of plasma species involved and the need of resolving electron kinetics, these chemical kinetic schemes are thus typically implemented within 0D (or 1D) frameworks [30,32]. Indeed, employing such schemes in multidimensional frameworks is impractical due to the high computational cost. However, accurately describing reactor performance requires not only resolving all relevant chemical processes, but also providing a detailed description of transport phenomena [33]. Consequently, multidimensional models must be developed to guide plasma reactor design and optimization.

Compared to the extensive number of 0D and 1D kinetic models available for air plasma, multidimensional fluid models are relatively scarce. Naidis and Babaeva [34,35] developed a 2D model for low-current glow and arc discharge columns in atmospheric-pressure air, describing laminar flow, while excluding the complex chemistry of electronically excited states.

Recently, multiple models have been developed that couple fluid flow and heat transfer in multidimensional models, while treating the chemical processes separately in 0D simulations, including only thermal chemistry [36,37] or incorporating a complete plasma set [38]. These 0D models rely on predefined trajectories and temperature profiles extracted from the multidimensional simulations. The thermophysical mixture properties used in the multidimensional simulations are often derived from equilibrium data from literature or interpolated from the results of the 0D chemical models. This methodology introduces significant approximations, as it neglects critical interactions, such as the endothermic and exothermic contributions of chemical reactions to heat transport, and the influence of chemistry on flow dynamics, e.g., dissociation reactions increase the number of particles, leading to gas expansion and altered flow fields. Most importantly, the strongest limitation of this decoupled approach is the neglection of diffusional transport between streamlines, a factor that can significantly impact conversion efficiency, as shown in more recent modeling studies [39–41].

Tatar et al. [1] recently measured the rotational and vibrational temperatures of a warm MW air plasma at 0.65 bar, demonstrating near vibrational-translational (V-T) equilibrium. These results suggest that resolving V-T non-equilibrium is unnecessary. In addition to the temperature measurements, Tatar et al. [1] performed 3D fluid simulations of the MW plasma reactor, incorporating full coupling of the gas flow field, heat and species transport, and thermal chemistry. Indeed, considering near V-T equilibrium and assuming that the rates of electron-impact processes are negligible compared to the high rates of thermal processes associated with the warm plasma temperatures ($T >$ 5000 K), the use of a simplified thermal chemistry set to describe the NO_x formation process is justified, eliminating the need to resolve electron kinetics and significantly reducing computational costs.

However, Tatar et al. [1] did not solve for the microwave field, but instead adopted a heat source with uniform power density, with its size and shape determined by analyzing light emission profiles from the reactor core. A drawback of this approach is the requirement for the heat source shape to be predefined, which restricts the model's predictive capabilities.

On the other hand, significant progress has also been made in the development of spatial models that do resolve the MW electric field by solving the wave equation based on Maxwell's equations, but for low pressure noble gas plasmas. Diaz et al. [42] developed a self-consistent 2D axisymmetric model of an argon plasma (8.8–20 mbar; 32–59 W), coupling fluid flow, heat transfer, electromagnetics, and electron energy balance. Another argon plasma model (2–26.7 mbar; 50–200 W) was built by Georgieva et al. [43]. Both models showed satisfactory agreement with the available measurements of electron density, electron temperature, and gas temperature as a function of pressure.

Compared to low-pressure, the modeling of MW plasma sources at atmospheric pressure is much more challenging, primarily due to the increased complexity of phenomena such as plasma contraction [44]. As a result, these models often exclude detailed chemistry, treating the working fluid as a single gas component or focusing on simple noble gas chemistry [43,45,46]. Some studies did model MW air plasma at atmospheric pressure, using varying approximations. Baeva et al. [47] developed a 2D model based on Maxwell's equations describing the electric field distribution, using a global kinetic model to calculate electron density, temperature, and species population densities for specified absorbed microwave power and gas temperature. Tatarova et al. [44] constructed a 1D model for a MW air plasma, employing a self-consistent approach that accounted for particle kinetics, gas dynamics, and wave electrodynamics, along with a comprehensive humid air plasma chemistry set. However, the 1D framework prevents it from resolving radial gradients and capturing important multidimensional effects, such as radial plasma contraction.

In this paper, similar to the recent work of Laitl *et al.* [48] for microwave CO_2 plasma, we present a newly developed fluid model describing (near-) atmospheric pressure air MW plasmas, resolving microwave field heating, turbulent flow, transport of heat and species, as

well as air thermal chemistry. As it was shown in [1] that sub-atmospheric pressure (0.65 bar) air MW plasma operates in near V-T equilibrium, we treat the mixture as a hot reactive gas and do not resolve electron kinetics, significantly reducing computational costs, and thus enabling for the first time the full coupling of chemistry, fluid dynamics and electromagnetics of atmospheric pressure air plasma within a 2D axisymmetric framework.

To validate the model, we compare its predictions against the experimental data from Tatar et al. [1], achieving good agreement in terms of NO_x production and gas temperature. Given that Tatar et al. [1] focused on a relatively low specific energy input (SEI < 52 kJ/mol) and sub-atmospheric pressure, we further assess our model calculations against the recent experiments of Troia et al. [2] who studied an open MW plasma torch for NF in air at atmospheric pressure over a broad range of power and flow rate conditions, demonstrating good agreement for the NO_x production rate across all conditions. The consistency between our model calculations and both experimental datasets for a broad range of conditions, without the need for experimental input data to parameterize (or finetune) the model, illustrates its predictive capabilities.

Based on our modeling insights, we aim to provide here a detailed mechanistic understanding of NO_x formation and destruction processes, as well as transport mechanisms, and how these mechanisms change as a function of SEI. In particular, we investigate the ideal operating conditions for thermal plasma-based NO_x formation, and identify the role of back reactions, and thus, in which SEI range active quenching, as in [49], is needed to maximize the NO_x yield. These valuable mechanistic insights provided by our new model, as well as its predictive capabilities, establish it as a valuable tool for optimization of plasma reactor design, and plasma-based NO_x production in future studies.

2. Model description

Our 2D axisymmetric model describes a vortex-stabilized air MW plasma and is developed in COMSOL Multiphysics™ [50], coupling the Reynolds-averaged Navier–Stokes (RANS) equations, transport equations of reactive chemical species (including their chemistry), the heat balance equation and wave equation defining the microwave field. To capture the correct swirl flow in the 2D axisymmetric model, we first perform a 3D Navier-Stokes calculation for air at ambient conditions (T = 293.15 K; p = 0.65 bar [1] or 1 atm [2]), and the resulting flow field is used to parameterise the tangential inlet in the 2D axisymmetric model, as discussed in section S.1 of the Supporting Information (SI). Below, we first present the geometry considered in the model (different for the benchmark experiments of [1,2]), while the model itself is the same for both benchmark experiments.

2.1. Geometry

For our first benchmark experiment performed by Tatar et al. [1], the model geometry follows the reactor setup described in [1], as illustrated in Fig. 1. The plasma reactor consists of a quartz glass tube with an internal diameter of 26 mm and outer diameter of 30 mm, which is inserted into a WR340 waveguide guiding 2.45 GHz microwave field. Air is introduced through two tangential inlets, each having an internal diameter of 1 mm. We note that the fully coupled 2D axisymmetric model employs a significantly longer simulation domain than the 3D flow model. This extension is necessary to allow the plasma effluent to cool to temperatures at which reaction kinetics are effectively frozen. We verified that enlarging the computational domain in the 3D model does not substantially affect the flow field near the inlet which is used to parameterize the tangential inlet conditions in the 2D axisymmetric model (see section S.1 in SI).

The second benchmark experiment conducted by Troia et al. [2] also investigates an open MW torch for NF, but differs in the method of MW plasma generation. The reactor comprises two resonators: a cylindrical, broad-band resonator and a coaxial, narrow-band resonator equipped with an ignition pin, as illustrated in Fig. 2. A more detailed description of the reactor setup is available in [2], although most reactor dimensions are not specified. All reactor dimensions were obtained through internal communication but are not disclosed here due to confidentiality considerations [51].

2.2. 3D gas flow model

The gas flow is described by the RANS equations, comprising the governing equations for total mass, momentum, turbulent kinetic energy k and specific turbulent dissipation rate ω:

$$\nabla \bullet (\overline{\rho}\overline{\boldsymbol{u}}) = 0, \tag{1}$$

$$\overline{\rho}(\overline{\boldsymbol{u}} \bullet \nabla)\overline{\boldsymbol{u}} = \nabla \bullet (-p\mathbf{I} + \mathbf{K}) \tag{2}$$

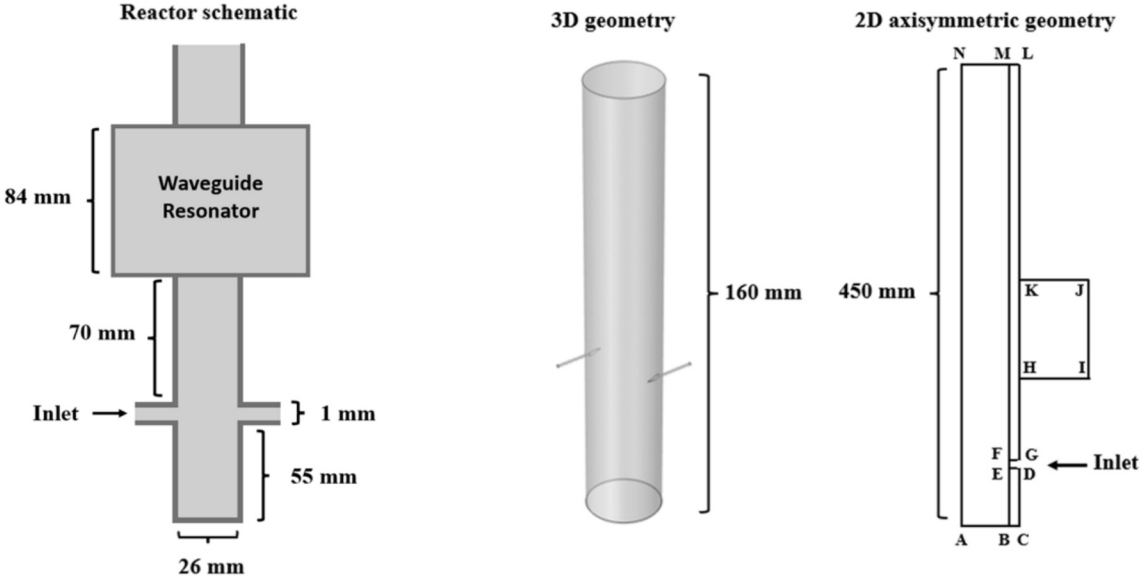

Fig. 1. Schematic drawing of the experimental reactor (left) of [1], the 3D model geometry (middle) and 2D axisymmetric geometry (right; the letters serve to explain the boundary conditions in Table S.1 of SI). In the 2D axisymmetric geometry, length ratios have been modified to improve clarity.

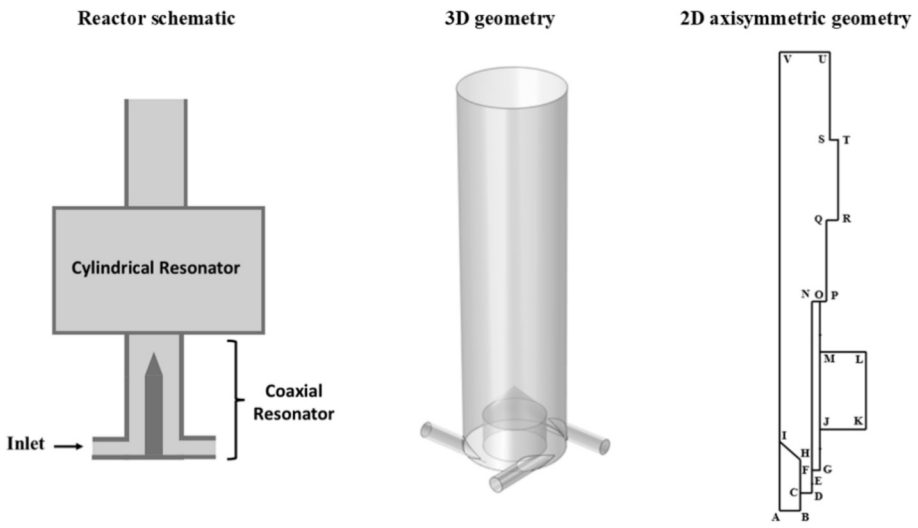

Fig. 2. Schematic drawing of the experimental reactor (left) of [2], the 3D model geometry (middle) and 2D axisymmetric geometry (right; the letters serve to explain the boundary conditions in Table S.2 of SI). In the 2D axisymmetric geometry, length ratios have been modified to improve clarity.

$$\overline{\rho}(\overline{\boldsymbol{u}} \bullet \nabla)k = \nabla \bullet ((\mu + \mu_T \sigma_k)\nabla k) + P_{lim} + \beta_0^* \overline{\rho}\omega k \tag{3}$$

$$\overline{\rho}(\overline{\boldsymbol{u}} \bullet \nabla)\omega = \nabla \bullet ((\mu + \mu_T \sigma_\omega)\nabla \omega) + \frac{\gamma}{\mu_T}\overline{\rho} P_{lim} - \beta_0^* \overline{\rho}\omega^2 + 2(1 - f_{v1})\left(\frac{\sigma_{\omega 2}\overline{\rho}}{\omega}\right)\nabla k \bullet \nabla \omega \tag{4}$$

Here, $\overline{\rho}$ denotes the Reynolds-averaged mass density and $\overline{\boldsymbol{u}}$ is the Reynolds-averaged velocity field, p is pressure, $\mathbf{I}$ represents the unity tensor and $\mathbf{K}$ is the friction tensor. The friction tensor $\mathbf{K}$ involves the dynamic and turbulent viscosity, and is formulated using the Menter shear stress transport (SST) model [52]. The SST model also provides the standard formulation of the scaling constants σ_k, σ_ω and γ, as well as the model constant $\beta_0^* = 0.09$ and the product-limiting coefficient P_{lim} [52].

In Section 4, the SST turbulence modeling results are compared with laminar flow calculations. For the latter, the balance equations for the turbulence variables (Eqs. (3)–4)) are omitted, and only the Navier–-Stokes equations (Eqs. (1)–(2)) are solved.

The inlet boundary condition is defined by the volumetric flow rate, assuming fully developed flow in the tangential inlets, and the outlet boundary is defined by setting the pressure equal to the working pressure p_0:

$$(-p\mathbf{I} + \mathbf{K})\boldsymbol{n} = -p_0 \boldsymbol{n}, \tag{5}$$

where $\mathbf{n}$ denotes the unit vector normal to the outlet plane.

2.3. Fully-coupled 2D axisymmetric plasma model

The gas flow is again described by the RANS equations (Eqs. (1)–(4) above) or Navier-Stokes equations in case of laminar flow (Eqs. (1)–(2)), now using a cylindrical coordinate system because of the 2D axisymmetric construction [40].

The model includes six chemically reactive species, namely N_2, O_2, N, O, NO and NO_2. Their transport and chemistry in the reactor is described by the conservation of mass:

$$\overline{\rho}(\widetilde{\boldsymbol{u}} \bullet \nabla)\widetilde{\omega}_i + \nabla \bullet \mathbf{j}_i = M_i R_i \tag{6}$$

in which i represents the given species, $\widetilde{\omega}_i$ is the Favre-averaged mass fraction, M_i is the molar mass and R_i is the reactive source term (mol m^{-3} s^{-1}). The first and second term in Eq. (6) account for convective and diffusive transport, respectively. The diffusive flux vector $\mathbf{j}_i$ is given by:

$$\mathbf{j}_i = -\left(\overline{\rho}(D_i + D_{T,i})\nabla\widetilde{\omega}_i + \overline{\rho}\widetilde{\omega}_i D_i \bullet \frac{\nabla M}{M} - \overline{\rho}\widetilde{\omega}_i \sum\nolimits_{k=species} \frac{M_k}{M} D_k \nabla \widetilde{x}_k\right) \tag{7}$$

where D_i is the mixture-averaged diffusivity, averaged over the binary diffusion coefficients calculated using the Chapman-Enskog theory [53]. $D_{T,i}$ denotes the turbulent diffusivity, obtained from the turbulent field by means of the Kays-Crawford theory [54], and M is the average molar mass. The last term on the right-hand side is a correction, ensuring that the total diffusive flux is zero. The correction is defined using the Favre-averaged mole fraction $\widetilde{x}_k$.

Table 1
List of chemical reactions involved in the reaction scheme, as well as the rate coefficients of the forward reactions (m^3 s^{-1} and m^6 s^{-1} for two-body and three-body reactions, respectively) and the references where the data is taken from. Temperature (T) is in K.

No.	Reaction	$k_{forward}$ (m^3 s^{-1}, m^6 s^{-1})	
(R1)	$N_2 + M \rightleftharpoons N + N + M^*$	$5.0 \times 10^{-14} \bullet \exp(-113200/T) \bullet (1 - \exp(-3354/T))$	[56]
(R2)	$O_2 + M \rightleftharpoons O + O + M$	$3.7 \times 10^{-14} \bullet \exp(-59380/T) \bullet (1 - \exp(-2238/T))$	[56]
(R3)	$N_2 + O \rightleftharpoons NO + N$	$3.0 \times 10^{-16} \bullet \exp(-38000/T)$	[55]
(R4)	$O_2 + N \rightleftharpoons NO + O$	$9.7 \times 10^{-21} \bullet T^{1.01} \bullet \exp(-3120/T)$	[55]
(R5)	$NO + M \rightleftharpoons N + O + M$	$2.4 \times 10^{-15} \bullet \exp(-74700/T)$	[57]
(R6)	$NO + O + M \rightleftharpoons NO_2 + M$	Lindemann falloff	[55]
(R7)	$NO_2 + O \rightleftharpoons NO + O_2$	$5.5 \times 10^{-18} \bullet \exp(188/T)$	[58]

* M = any neutral.

The reactive source term R_i represents the production and loss rates of the species due to chemical reactions, and is calculated according to the reaction scheme listed in table 1. The reactions included in the model are N_2, O_2 and NO dissociation (R1, R2, R5), the Zeldovich reactions (R3, R4), NO oxidation (R6) and NO_2 destruction by O atoms (R7). Table 1 presents the rate coefficients of the forward reactions. All reverse rate coefficients are calculated according to the principle of detailed balance, where the equilibrium constant is calculated from the Gibbs free energy of the reaction. An exception is made for reaction (R6), where the equilibrium constant is specified according to the fit described in [55]. Reactions R1, R2, R5 and R6 use a third body (M). The third body efficiencies for atomic species N and O are set to 2.2 for reaction (R1) and 3.5 for reaction (R2) [56], the third body efficiency for N_2 is set to 0.25 for reaction (R2), while the third body efficiencies for all other molecular species are assumed to be unity across all reactions.

Additional reactions involving relevant species were evaluated during model development. These reactions were found to have negligible impact on the overall NO_x concentration and were excluded due to the associated uncertainties in rate coefficient data across the broad temperature range (300–5000 K) and the added complexity, which would reduce the interpretability of the simulation results.

A sensitivity analysis was conducted to evaluate the impact of experimental uncertainties in the Zeldovich reaction rate coefficients (R3 and R4) reported in [55]. Each reaction rate coefficient was individually varied within the reported uncertainty bounds, by either multiplying or dividing the values by a factor two. The largest deviation was observed when modifying the rate coefficients of R3 and R4 under high SEI conditions, resulting in a NO_x concentration ranging from 2.21 % to 2.46 % (when varying R3), and from 2.18 % to 2.50 % (when varying R4), for a flow rate of 6 slm and SEI = 132 kJ/mol.

Transport of heat within the reactor is described in the heat balance equation:

$$\bar{\rho}C_p(\tilde{\boldsymbol{u}}\bullet\nabla)T+\nabla\bullet(-(\lambda+\lambda_T)\nabla T)=\sum_{j=\text{reactions}}-r_jH_j^0+\sum_{i=species}-\mathbf{j}_i\bullet\nabla\frac{H_i^0}{M_i}+\dot{q_{rh}} \tag{8}$$

Here, C_p is the mixture-averaged isobaric heat capacity, λ and λ_T are the molecular and turbulent thermal conductivity (Kays-Crawford [54]), respectively, and r_j and H_j^0 are the reaction rate and enthalpy, respectively. The last term, $\dot{q_{rh}}$, describes the rate of microwave field heating. This term is directly incorporated into the heat balance equation, as it is assumed that, due to fast electron energy relaxation in molecular gases [59,60], the electron energy transfer is entirely local and is expressed as:

$$\dot{q_{rh}}=\frac{1}{2}Re(\sigma\boldsymbol{E}\bullet\boldsymbol{E}^*) \tag{9}$$

Here, σ is the electrical conductivity of the system, $\boldsymbol{E}$ is the electric field, and * denotes a complex conjugate. The $\boldsymbol{E}$ vector is calculated as an eigenvector of the wave equation:

$$\nabla\times\mu_R^{-1}(\nabla\times\boldsymbol{E})=\kappa_0^2\left(\varepsilon_R-\frac{\boldsymbol{i}\sigma}{\omega_s\varepsilon_0}\right)E \tag{10}$$

In eq. (10), $\omega_s=2\pi\bullet 2.45$ GHz is the angular frequency of the source, $\kappa_0=\frac{\omega_s}{c_0}$ is the vacuum wavevector (c_0 = 299792458 m s^{-1}). The magnetic permeability μ_R is equal to 1 for non-magnetized plasma [61] and approximates 1 for the quartz tube [50]. The expression $\left(\varepsilon_R-\frac{\boldsymbol{i}\sigma}{\omega_s\varepsilon_0}\right)$ describes the complex relative permittivity of the plasma, where ε_R is the real part of the dielectric constant. By convention, $\varepsilon_R = 1$ in the discharge domain [61]. For the quartz tube (fused silica), the $\varepsilon_R = 3.6$ and $\sigma(T)$ values are used as given in [62,63].

The microwave power is fed from the port boundary, as explained in section S.1 of the SI. The correlation used (Table S.3 and S.4) refers to a transverse electromagnetic (TEM) mode, which allows the most efficient power coupling to the plasma column [64]. In our model, Eq. (10) only accommodates axisymmetric wave modes due to the 2D axisymmetric geometry. We note that, however, recent work [65] demonstrated that 2D axisymmetry effectively describes microwave propagation when the reactor radius is sufficiently small, preventing nonaxisymmetric higher order modes to propagate. This condition is met in our reactor setup.

The electrical conductivity of the discharge is defined as:

$$\sigma=\frac{N_e e^2}{m_e\left(\nu_m+\boldsymbol{i}\omega_s+\frac{\omega_s}{10}\right)} \tag{11}$$

where e is the elementary charge, m_e is the electron mass, N_e is the electron number density and ν_m is the electron-neutral collision frequency. The last term in the denominator of eq. (11) improves numerical convergence [66].

In this work, N_e and ν_m are obtained from local thermodynamic equilibrium (LTE) calculations, similar to the approach in [67], and not calculated self-consistently by solving a complete plasma kinetic scheme. This choice is motivated by the strong alignment between model and experiment for NO_x production using the equilibrium properties.

At the lower specific energy inputs (SEIs) investigated in this study (i.e., < 30 kJ/mol), the assumption of LTE electron densities may introduce more significant errors due to the increased non-equilibrium nature of the MW plasma in this regime. This could partly explain the overcontracted temperature profile observed when modeling the setup from [1] using the SST turbulence model, as will be discussed in section 4.1.1 below.

The observed agreement when using the equilibrium conductivity suggests that the conductivity is relatively insensitive to the elevated electron temperature in regions where field heating predominantly occurs. A possible explanation is the presence of the efficient associative ionization (AI) pathway in air plasma, i.e., $N + O \rightleftharpoons NO^+ + e$ [68]. Compared to for example thermal CO_2 plasma, where AI is also the most efficient ionization process, the dominant AI channel is $C + O \rightleftharpoons CO^+ + e$ [69], occurring considerably slower than the dominant AI process in air. This is illustrated by the following Gibbs free reaction energies, calculated using the NASA 9 polynomials [70]:

$½\ N_2 + ½\ O_2 \rightarrow NO^+ + e\ \Delta G^0 = 9.5$ eV.

$CO_2 \rightarrow ½\ O_2 + CO^+ + e\ \Delta G^0 = 16.7$ eV.

The rate of AI is expected to increase under elevated electron temperatures due to the population of electronically excited states of the atomic species involved in the AI process [68], and possibly atom generation through electron impact dissociation. However, owing to the lower ionization barrier for air, the non-equilibrium ionization enhancement is likely to be less pronounced compared to for example CO_2 plasma. This results in the conductivity being relatively insensitive to elevated electron temperature already at lower gas temperatures [34], potentially explaining why the equilibrium conductivity yields a reasonable description of MW field heating in our model. This

hypothesis could be validated through electron density calculations using an extensive plasma kinetic scheme that describes warm air plasma. If validated, it would allow accurate physical predictions of warm air plasma without resolution of the complex electron impact processes, which significantly reduces the complexity and computational cost of multidimensional simulations.

The thermodynamic equilibrium values for N_e are obtained from Gibbs free energy minimization calculations in CANTERA [71], using the NASA 9 polynomials [70] to calculate thermodynamic properties. The equilibrium calculations include the neutral species involved in our kinetic scheme (see Table 1), as well as the charged species NO^+, O_2^+, O^+, N_2^+, O_2^- and O^-. The electron collision frequency is calculated for each neutral species as an integral over the electron cross-sections, according to:

$$\nu_m = \sqrt{\frac{2}{m_e}} \sum_i N_i \int_0^\infty f(E)\sigma_i(E)E dE \tag{12}$$

Here, N_i is the density of neutral species i at equilibrium, f is the electron energy distribution function (EEDF), assumed to be Maxwellian following thermodynamic equilibrium, σ_i is the electron-neutral momentum transfer cross-section and E is the electron energy. The IST-Lisbon database is used for O_2 and N_2 [72], the Morgan database for O and N [73], where the sum of the elastic and all inelastic processes is made due to lack of effective cross-sections, and the Phelps database for NO [74], where all are obtained from the LXCat database. The integrations over the EEDF are performed in CANTERA [71].

Interpolating the electron density and collision frequency from LTE calculations is an approximation within our model. This approach neglects the role of electronically excited states in enhancing AI processes, which, as discussed above, is expected to be limited under the present conditions. Furthermore, it does not account for ambipolar charge fluxes, as the Poisson equation is not solved and ion transport is omitted. The influence of ambipolar fluxes on the electron density profile is expected to be minor due to rapid dissociative recombination associated with the high charge densities typical of warm, near-atmospheric pressure microwave plasmas [30]. This approximation is evaluated in the SI, section S.2.

In addition to neglecting electron transport, deriving the electron density from LTE calculations also implies neglecting the deviations in the heavy species composition from equilibrium due to transport. This effect is likewise expected to be limited, as species fractions within the plasma region remain close to their equilibrium values. Significant deviations are only observed in lower temperature regions near the periphery or in the effluent. The most pronounced deviation within the plasma is observed for the O atom density, whose density is approximately 25 % lower than its equilibrium value due to diffusive losses. Consequently, the impact of heavy species transport on the electron density is expected to be minimal.

While these effects are expected to be limited under the high gas temperatures and near-atmospheric pressure conditions considered in this study, they may still affect plasma conductivity under low SEI conditions and, consequently, the interaction between the plasma and the MW field. In future work, we aim to extend the model within a quasineutral framework that incorporates electron impact chemistry, ion transport, and electron energy transport, enabling a more accurate assessment of these effects.

The complete set of governing equations is closed by the set of boundary conditions listed in Tables S.1-S.4 in the supporting information.

3. Results and discussion

We begin by validating our model against the experimental measurements of Tatar et al. [1], comparing the calculated temperature profiles and NO_x production. Subsequently, we assess our model predictions for NO_x concentration and electron density against the experimental data of Troia et al. [2]. After validation, we investigate the mechanisms contributing to NO_x production, considering both chemistry and transport effects.

3.1. Comparison against open MW torch NF experiments at 0.65 bar and 20 slm

3.1.1. Temperature profile

The axial temperature profile along the symmetry axis, as well as axial profiles at radial distances of 3 mm and 6 mm from the symmetry axis, are presented in Fig. 3 for both the modeling calculations (solid lines) and discrete experimental measurements (circles). The modeling calculation incorporating turbulent effects via the SST model is shown on the left (Fig. 3a). The experimentally determined maximum axis temperature of 5700 K ± 550 K is well captured by the model. Furthermore, the axial temperature profiles suggest that the model reasonably reproduces the axial position of the discharge. However,

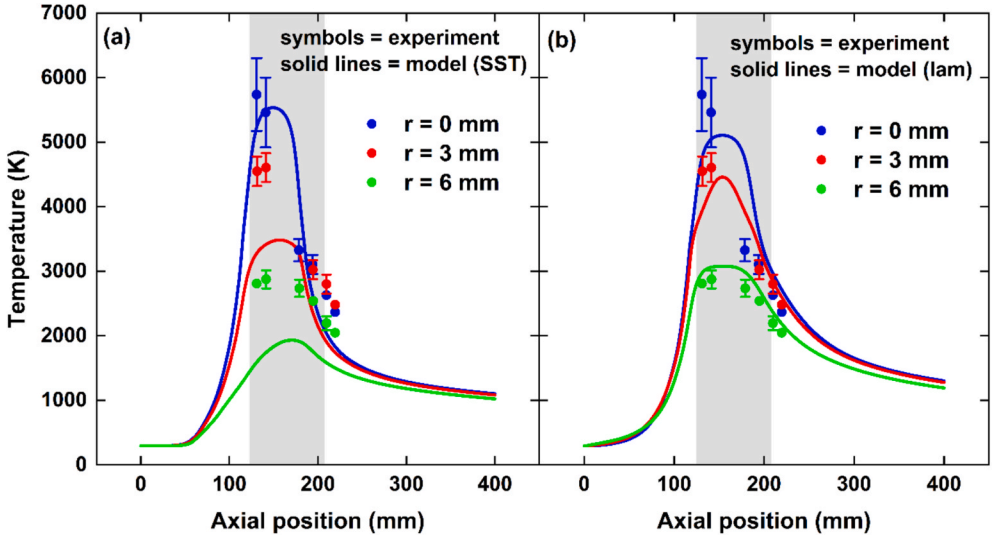

Fig. 3. Experimental temperature measurements (circles) and calculated temperature profiles (solid lines) as a function of axial position, for different radial distances from the symmetry axis, at a power of 400 W and flow rate of 20 slm. Modelling calculations using the SST model and assuming laminar flow are shown on the left (a) and right (b), respectively. The grey rectangle denotes the region covered by the waveguide.

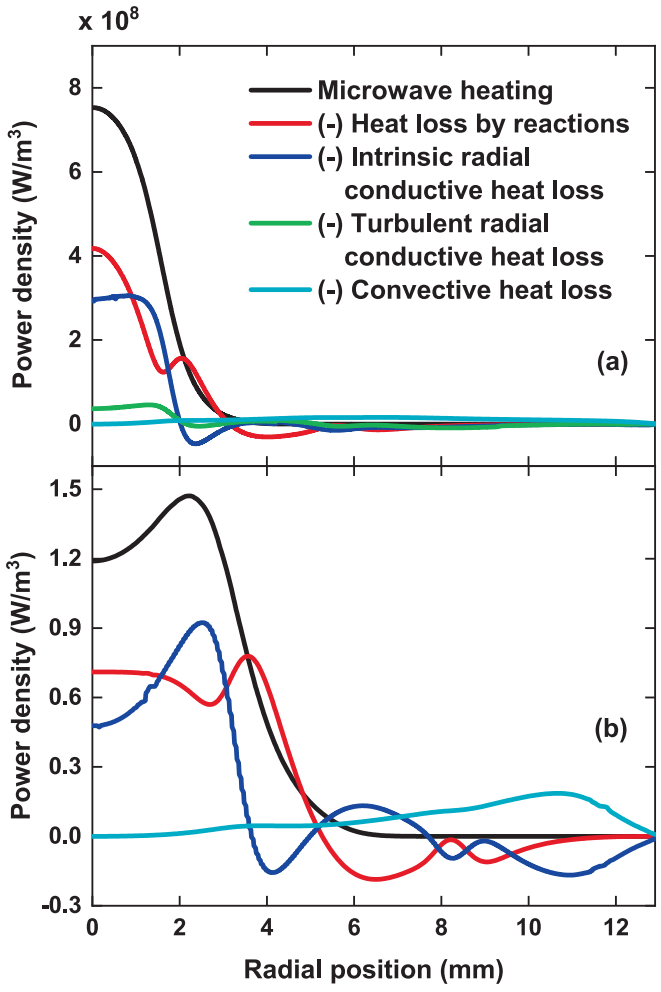

Fig. 4. Dominant heating and cooling terms in the heat balance for the SST model (a) and laminar model (b) (400 W; 20 slm), as a function of radial position, for an axial position of 150 mm from the bottom of the reactor, corresponding to the maximum gas temperature. The red, blue and green curves represent loss as positive values, while negative values represent heating.

beyond approximately 180 mm along the axial direction, the calculated temperature declines slightly more rapidly. Additionally, while the model accurately predicts the maximum temperature at the axis, it significantly underestimates the temperature at radial positions of 3 mm and 6 mm, with maximum deviations of approximately 1200 K and 1000 K near the axial centre of the discharge at r = 3 mm and r = 6 mm, respectively.

Fig. 3 (b) presents the axial temperature profiles from the modeling calculation assuming laminar flow. While the laminar flow model slightly underestimates the maximum axis temperature, the predicted value of 5080 K is still reasonably close to the experimental uncertainty range of 5700 K ± 550 K. However, compared to the SST model, the laminar flow calculation more accurately captures the temperature decline toward the end of the discharge. Furthermore, the calculated axial temperature profiles at r = 3 mm and r = 6 mm are close to the measured temperatures, indicating that the laminar flow model seems to more accurately represent the experimental plasma radius.

The enhanced plasma contraction in the SST model mainly arises from increased thermal conductivity, owing to the additional contribution of turbulent thermal conductivity λ_T (see equation (8) above), which is proportional to the turbulent kinetic energy that is generated near the edges of the plasma [75].

In stationary conditions, the power balance requires that MW heating equals the total heat losses due to transport and chemical processes. Fig. 4 illustrates the dominant heating and cooling terms in the heat balance (see equation (8) along the radial cut line at axial position z = 150 mm, including MW heating, heat released or absorbed by chemical reactions, radial conductive heat loss and convective heat loss for the SST (a) and laminar flow (b) model. For the SST model, the radial conductive heat loss is decomposed into intrinsic conductive losses, based on molecular thermal conductivity, and a turbulent contribution arising from enhanced mixing. Radial and axial convective heat transport are grouped together, while axial conductive heat loss is omitted due to its negligible contribution.

As shown in Fig. 4 (a), the turbulent contribution to radial conductive heat removal is relatively small but non-negligible. To compensate for this additional loss, the plasma contracts to increase power density deposition, as seen by the significantly higher peak power density deposition (microwave heating) for the SST model, i.e., 7.5×10^8 W/m^3, compared to 1.5×10^8 W/m^3 for the laminar model. However, the reduced plasma radius steepens the radial temperature gradient, further enhancing conductive heat losses. This interplay creates a feedback loop that stabilizes the plasma radius at a point where MW heating and heat removal are balanced. Due to this thermal instability [76,77], even a modest increase in radial conductive heat losses from turbulence can lead to significant changes in plasma radius.

When we rerun the SST calculation (400 W; 20 slm) with the turbulent thermal conductivity λ_T set to zero, the plasma expands, following the reasoning above. However, the radial temperature profile is still slightly more contracted than that of the laminar flow calculation, as shown in Fig. S.4 of the SI. This indicates that there is also a small contribution of enhanced convective heat loss associated with the turbulent velocity field in the power balance that forces the plasma to contract in the SST model, albeit to a lesser extent than the enhanced radial conductive losses. This discussion therefore explains why the plasma is significantly more contracted when turbulent velocity effects are considered (cf. Fig. 3(a) vs. Fig. 3(b)).

Although thermal plasma generally induces a turbulent flow field due to strong gradients in temperature, velocity, and chemical composition near the plasma edges [75], the laminar flow model exhibits better agreement with experimental results than the SST model. A possible explanation is that turbulent effects for the vortex-stabilized air MW plasma have minor impact at the current pressure and SEI, and that the parameterization of the SST model is not well-suited to accurately describe this system, leading to an overestimation of turbulent kinetic energy production and its related transport effects. Consequently, this results in excessive heat removal and over-contraction of the plasma.

Another possible explanation for the discrepancy between the SST model and experimental results is a suboptimal characterization of MW field heating. In the simulation, electrical conductivity is determined from the electron density under the assumption of local thermodynamic equilibrium (LTE) at the given gas temperature. However, the LTE assumption may not adequately capture the behavior of the present system. Specifically, the relatively low SEI (26.9 kJ/mol or 0.28 eV/molecule) may cause the plasma to deviate too strongly from thermodynamic equilibrium, necessitating the resolution of elevated electron temperatures. These elevated electron temperatures enhance AI via the generation of electronically excited atomic species [68], increasing the electron density at lower gas temperatures, situated more towards the plasma edge. Additionally, the LTE assumption neglects ambipolar ion fluxes, which could be of significance under the reduced pressure and low SEI. These fluxes can similarly increase the electron density near the plasma edge due to outward transport from the hot plasma core.

Both elevated electron temperature and ambipolar ion fluxes would enhance the electrical conductivity at lower gas temperatures, resulting in more uniform plasma heating and an expanded plasma region. Therefore, neglecting these effects may lead to overcontraction of the plasma under low SEI conditions. In the future, it might therefore be useful to develop a fully coupled multidimensional plasma model incorporating electron kinetics and ion transport to assess the validity of

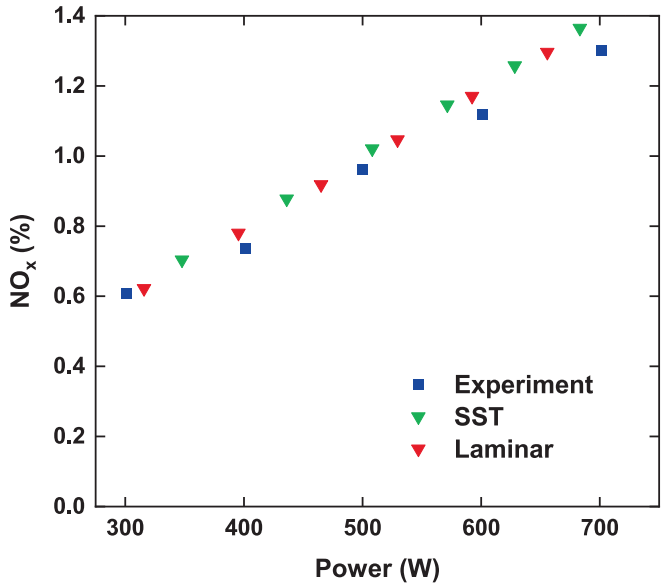

Fig. 5. NO_x molar concentration evaluated at the reactor outlet in the experiment and modelling calculations assuming turbulent (SST) and laminar flow.

the LTE conductivity assumption. However, such an approach remains challenging due to its high computational cost.

At present, it is unclear whether the improved agreement with the experimental temperature profile when using the laminar flow model arises from a more physically accurate representation of the flow field and transport effects, or from error compensation for the overcontracted plasma resulting from the LTE-based electron density approximation under low SEI conditions. Further investigation is required to assess the validity of RANS-based models, such as SST, in capturing the turbulent flow characteristics of thermal plasmas under the current operating conditions. This should be pursued through comparison with carefully designed experiments or higher-level turbulence modeling approaches, such as Large Eddy Simulations.

3.1.2. NO_x production

In Fig. 5 we compare the calculated and measured NO_x molar fraction at the outlet, defined as the sum of the NO and NO_2 molar fractions, as a function of input power. The modelled NO_x molar fraction, x_{NO_x}, is averaged over the outlet boundary, according to:

$$x_{NO_x} = \frac{2\pi \int v_{ax} \bullet \rho(r)[\omega_{NO}(r)/M_{NO} + \omega_{NO_2}(r)/M_{NO_2}]rdr}{2\pi \int v_{ax} \bullet \rho(r)/M_n(r)rdr} \quad (16)$$

where v_{ax} is the axial velocity, ρ is the mass density, ω_{NO} and ω_{NO_2} are the mass fractions of NO and NO_2, M_{NO} and M_{NO_2} are their respective molar masses, and M_n is the mean molar mass of the mixture.

Both the SST model and the laminar flow model exhibit close agreement with experimental results across the entire power range, demonstrating that the model accurately predicts NO_x production. Therefore, while the turbulent flow field strongly influences plasma shape and temperature, it has a minimal impact on chemical conversion. These findings further support the conclusion from [78] that chemical conversion is relatively insensitive to the temperature profile for MW CO_2 plasma.

The observation that the more contracted plasma obtained under turbulent flow conditions yields nearly identical final NO_x concentrations compared to the broader plasma predicted for laminar flow can be attributed to two compensating effects. Specifically, the smaller chemically reactive region in the turbulent case reduces overall NO production, while the faster transport enhances net NO production.

Fig. 6 shows the radial temperature profile at the axial position corresponding to the maximum plasma temperature for both turbulent (SST) and laminar flow assumptions (left y-axis), along with the net NO production rate (R_{NO}), i.e., sum of the rates of all production minus loss reactions involving NO (right y-axis). Both models exhibit a peak in net NO production rate near 3850 K, however, the SST model predicts a significantly higher maximum rate, located closer to the axis compared to the laminar model, i.e., the peak occurs at r = 2.4 mm with $R_{NO} = 183$ mol m^{-3} s^{-1} and at r = 4.1 mm and $R_{NO} = 57$ mol m^{-3} s^{-1} for the turbulent and laminar case, respectively.

As discussed in detail in Section 4.3.2, the net production rate is primarily balanced by radial diffusive transport. The combination of sharper radial gradients in NO concentration associated with the more contracted plasma for the SST calculations, and turbulence-enhanced diffusion leads to stronger radial transport compared to the laminar flow calculations. At the radial position of peak NO production, the effective diffusion coefficient of NO, including turbulent diffusivity, is approximately 30 % higher than the molecular diffusivity (cf. Equation (7). This enhanced transport accommodates the higher net NO production rate predicted by the SST model.

In contrast, the laminar flow calculation exhibits a lower net production rate, but NO formation occurs at larger radial positions due to the broader temperature profile, occupying a greater volume under cylindrical geometry. This larger production volume compensates for the lower local production rate, resulting in similar final NO concentrations for both flow assumptions. Therefore, while the choice of turbulence model significantly influences the mechanisms of NO formation and the local NO production rates, the final NO_x concentration remains largely unaffected within the investigated range of conditions due to these compensating effects.

We note that in [1], NO_x concentration measurements were conducted down to an input power of 100 W. However, at these very low SEI values, the microwave power fails to couple to gas heating in the modeling calculations, likely due to the inaccuracy of the LTE conductivity assumption at these very low SEIs, as previously discussed. Consequently, no modeling results are available for input powers below 350 W.

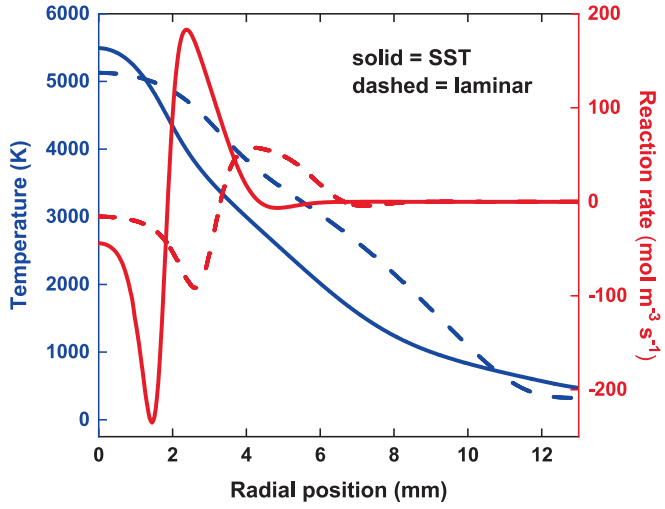

Fig. 6. Temperature (left y-axis) and net total reactive source term of NO, i.e., sum of the rates of all production minus loss reactions involving NO, on the right y-axis (400 W; 20 slm), as a function of radial position, at the axial position corresponding to the maximum plasma temperature, i.e., z = 149 mm and z = 154 mm for turbulent and laminar flow, respectively.

3.2. Comparison against open MW torch NF experiments at 1 atm

Since the study by Tatar et al. [1] focused on relatively low specific energy inputs (SEI < 52 kJ/mol), we further validate our modeling

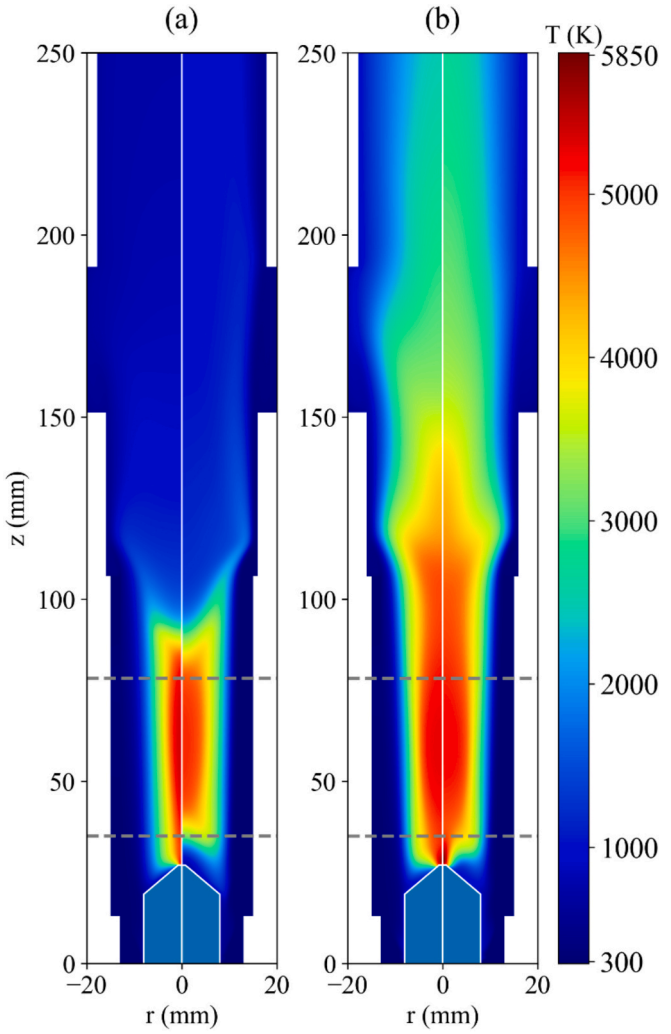

Fig. 7. Calculated temperature profiles for a flow rate of 60 slm and power of 600 W (a) and a flow rate of 40 slm and power of 1350 W (b). In each plot, the results of the SST model and laminar flow model are shown in the left-hand side and right-hand side, respectively.

results against the recent experiments by Troia et al. [2], which investigated open MW torch NF at atmospheric pressure across a broad range of power (545–2000 W) and flow rates (5–90 slm), corresponding to an SEI range of ca. 10–400 kJ/mol.

3.2.1. *Temperature profile*

It was demonstrated in section 4.1 that the choice of turbulence model, i.e., laminar or SST, has minimal influence on the NO_x production rate, i.e., product of final NO_x concentration and total molar flow rate, but significantly affects the predicted temperature profile. Although no temperature measurements were reported in [2], we extend our analysis by comparing the calculated temperature profiles using both the laminar and SST models under the reactor conditions described in [2].

Fig. 7 compares the temperature profiles obtained using the SST model and laminar flow model, for a low SEI of 14.8 kJ/mol with a flow rate of 60 slm and power of 600 W (a) and a moderate SEI of 49.9 kJ/mol with a flow rate of 40 slm and power of 1350 W (b). In the low SEI scenario (a), the temperature profiles differ strongly between the two models, in line with section 4.1.

Indeed, as observed in our simulations of the setup in [1] (section 4.1.1), laminar flow yields a broader temperature distribution. This is related to the higher power absorption by the plasma in the radial direction, reducing the power carried by the surface wave toward the pin or the outlet. Hence, a shorter plasma column is obtained in the laminar flow model. Due to the absence of experimental temperature measurements or CCD imaging, it remains uncertain which temperature profile is more physically accurate.

Fig. 7 (b) shows the temperature profiles at a moderate SEI of 49.9 kJ/mol, where differences between the SST and laminar flow models are notably weaker. This reduced sensitivity to the inclusion of turbulent effects can partly be attributed to the larger plasma zone with elevated temperatures and increased viscosity. For applications targeting high NO_x production rates with low EC, SEIs in the range of 50 – 100 kJ/mol are preferred, as they enable high NO_x concentrations without exceeding the saturation threshold [2]. Therefore, within this relevant SEI range and moderate flow rates (< 40 slm), the modeling results indicate that the choice of turbulence model has limited impact on the calculated temperature profile. However, combinations of higher power and flow rates yielding similar SEIs, may exhibit stronger dependence on turbulence effects.

As shown in Fig. 7, the plasma attaches to the ignition pin at z = 27 mm under most conditions, which was also frequently observed in experiments [51]. Only at the lowest SEIs, the plasma detaches from the pin in the laminar flow model (cf. Fig. 7 (a) right panel). The plasma attachment to the pin is non-trivial, as one might expect plasma formation to occur primarily within the broad-band resonator, where the electric field of the TE_{010} mode reaches its maximum [79]. Indeed, the ignition pin was solely designed to ignite the discharge [79]. However, once the plasma is ignited, it allows a conversion of the propagating microwave mode in order to sustain a surface wave discharge [42,80]. The observed extension of the plasma toward the pin in the model, outside the resonator chamber, is likely the result of surface wave propagation upstream, as the plasma also attaches for the lower flow rate conditions where backflow near the pin is negligible.

At lower SEI values, where the plasma column is shorter, the axial backflow likely contributes to pushing the plasma toward the pin. The observation that the plasma attaches in the SST model but not in the laminar flow model at these conditions is thus likely due to a combination of a longer plasma column, and significant backflow reaching the pin in the SST model (see Fig. S.5 in the SI), which is absent in the laminar case. Supporting plots of the electric field and microwave heating are provided in the SI (Fig. S.6).

As discussed above, differences in the predicted temperature profiles between the laminar and turbulent SST models are only significant at relatively low SEI values (e.g., 15 kJ/mol). As demonstrated in Section 4.1.2 for the setup described in [1], the choice of turbulence model has a negligible impact on NO_x production, which is confirmed in Section 4.2.3 for the setup of [2]. In subsequent sections, where no direct comparison between the laminar and turbulent flow models is made, and without strong reasons to prefer one over the other, we adopt the SST model. This choice is motivated by the general expectation that thermal plasmas induce turbulent flow fields [75]. In addition, RANS models such as SST are typically better suited for capturing the dynamics of swirling flows compared to laminar models [81]. Finally, we encourage avoiding the use of laminar flow models in systems that exhibit stronger turbulence than those considered here, such as nozzle expansion chambers [82], where resolution of turbulent effects may be essential for accurately representing the flow physics.

3.2.2. *Electron density*

In addition to the NO_x measurements, electron density measurements were performed in [2] via microwave interferometry. Assuming a Gaussian electron density distribution profile, the maximum density can be obtained from the measured phase shift and estimated plasma radius, according to [2]:

$$n_{e,max} = 2\frac{1}{d}\frac{\lambda n_c}{\pi}\Delta\Phi \tag{17}$$

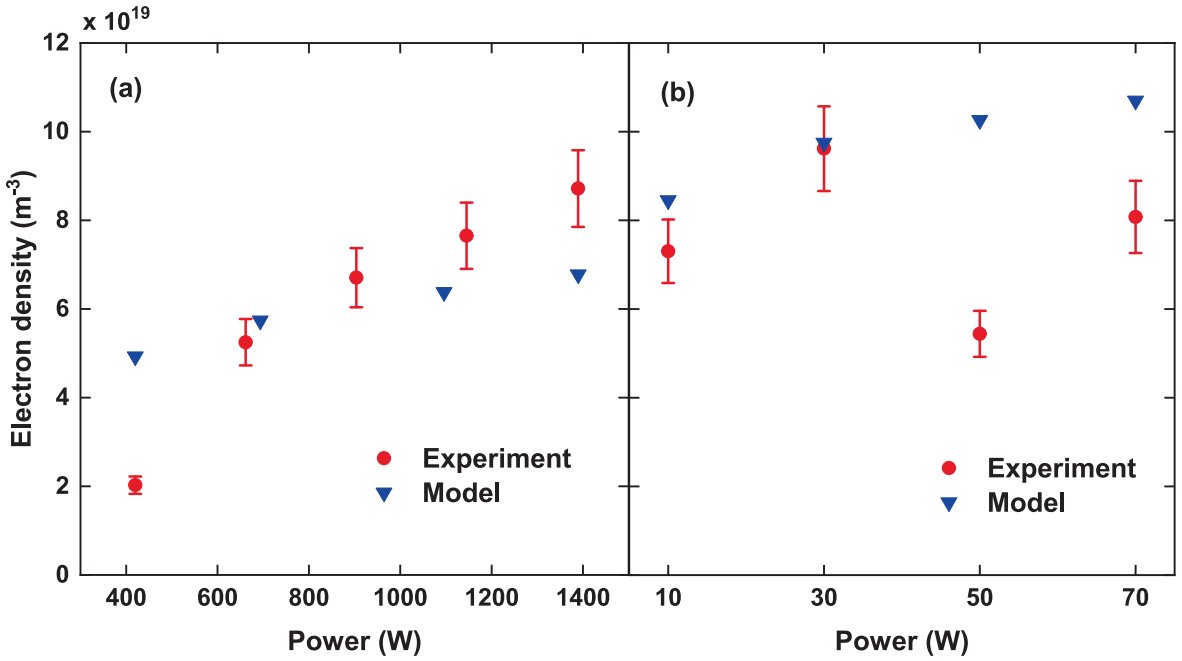

Fig. 8. Electron density as a function of power, for a constant flow rate of 14 slm (a), and electron density as function of flow rate, for a constant power of 1140 W (b). The modeling predictions are obtained assuming turbulent (SST) flow.

where d is the plasma radius, λ is the probing beam wavelength, n_c is the critical electron density and $\Delta\Phi$ is the phase difference.

Multiple studies have measured that the electron density at the core of atmospheric pressure MW plasmas in molecular gases corresponds to the LTE electron density [77,83,84]. Consequently, $n_{e,max}$ is uniquely linked to the temperature at the symmetry axis, assuming the temperature profile has its maximum at r = 0. Therefore, we can compare the maximum electron density obtained from LTE calculations at the symmetry axis to $n_{e,max}$ measured in the experiment, to indirectly validate whether the temperature at the symmetry axis is correctly predicted.

Fig. 8 compares the calculated electron densities for the SST model at the symmetry axis to the experimental measurements as a function of power for a constant flow rate of 14 slm (a), and as function of flow rate for a constant power of 1140 W (b). For the simulations at constant power, we ensured that the absorbed plasma power in the model does not deviate more than 3 % from 1140 W. The axial position at which the maximum electron density is evaluated in the model is taken to be the middle of the resonator, corresponding to the line of sight of the interferometer [2].

For intermediate powers in Fig. 8 (a), the calculated electron densities lie close to the experimental error ranges, which illustrates strong agreement considering the sensitivity of LTE-based electron densities to the modeled temperature (e.g., electron densities of 2×10^{19} and 5×10^{19} m^{-3} correspond to temperatures of 4450 and 4850 K, respectively).

The experimentally observed increase in electron density with power (a) is stronger than predicted by the model, resulting in a higher value calculated by the model at 400 W and a lower calculated value at 1400 W. In the experimental setup, the plasma radius was estimated from camera imaging and assumed constant across all power levels [2], due to the absence of more precise diagnostic techniques such as laser spectroscopy. In contrast, the model shows that with increasing power, the plasma expands both axially and radially, which leads to a substantial increase in plasma radius and only a moderate rise in plasma core temperature, as is characteristic to near-atmospheric pressure MW plasma [85]. However, as shown in Eq. (17), the experimentally derived electron density is inversely proportional to the plasma radius d. Hence, if the plasma radii were assumed to increase with power, $n_{e,max}$ would likely exhibit a weaker increase, thereby improving agreement between model and experiment.

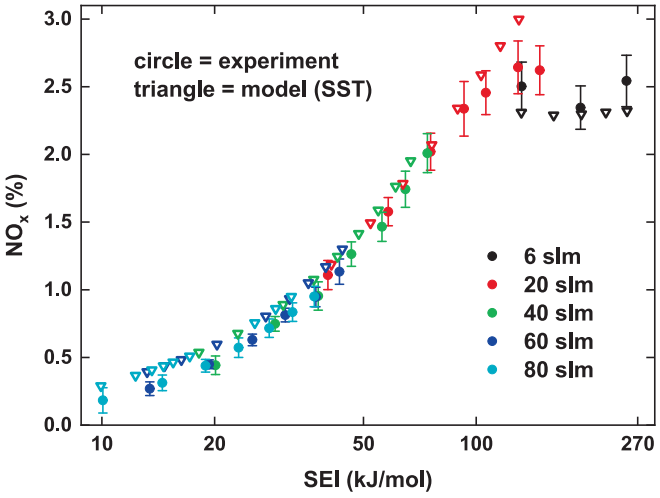

Fig. 9. NO_x molar concentration as a function of SEI, measured or calculated using the turbulence SST model. Note that the x-axis is logarithmic, as most data lies within the lower SEI range (< 100 kJ/mol), where the NO_x concentration does not saturate.

Fig. 8 (b) shows no clear trend in the experimentally measured electron densities with increasing flow rate. In contrast, the model predicts a relatively weak increase in electron density upon rising flow rate. This behavior is attributed to enhanced turbulent kinetic energy production at higher flow rates, which leads to increased radial conductive heat losses (see Section 4.1.1), as well as greater convective heat losses due to the higher gas velocity. According to the power balance discussed in Section 4.1.1, higher microwave power deposition is required to compensate for these increased losses, which corresponds to slightly elevated core plasma temperatures and electron densities.

Similarly to the observed plasma expansion with rising power and SEI when modeling the conditions in Fig. 8 (a), the plasma contracts both axially and radially as the SEI decreases with increasing flow rate at

constant power. Since a constant plasma radius is assumed in the experimental analysis, the electron density is likely underestimated at higher flow rates, which may explain why the weak increase predicted by the model is not reflected in the measurements. Nevertheless, considering the overall agreement, we believe the model reasonably predicts the core electron densities, and hence the core plasma temperatures.

3.2.3. No_x production

Fig. 9 compares the NO_x molar fraction at the outlet between model predictions and experimental data as a function of SEI for various molar flow rates. As in our modeling of the setup in [1] (section 4.1.2), the SST and laminar flow results are closely aligned; therefore, only SST results are shown here, with laminar flow data included in the SI (Fig. S.7). For SEI values below 100 kJ/mol, the model accurately reproduces the experimentally observed linear increase in NO_x concentration with input power, with calculated values close to the experimental error margins.

Above SEI values of approximately 100 kJ/mol, the experimental data (6 and 20 slm) show a saturation in NO_x concentration, stabilizing around 2.5 % despite increasing power. This saturation is not yet observed in the model at 20 slm, as indicated by the final data point at 142 kJ/mol, where the NO_x concentration reaches 2.9 %. At this high SEI, the outlet gas temperature in the model remains sufficiently elevated to sustain a reactive mixture. In such a mixture, NO reacts back to N_2 and O_2, as shown by the negative axial gradient in NO_x concentration near the outlet boundary in the model. Therefore, if a larger simulation domain is modelled, the NO_x concentration at the outlet boundary would decrease due to the reverse Zeldovich reactions occurring upon cooling of the mixture. The current discrepancy is thus a result of the limited computational domain, which was selected for computational efficiency. When we increase the simulation domain along the axial direction for the condition of SEI = 142 kJ/mol and flow rate of 20 slm, the NO_x concentration drops to 2.0 %, matching the upper limit observed at 6 slm, as discussed in the following paragraphs. The axial NO_x concentration in the plasma effluent for the extended simulation domain is presented in Fig. S.8 of the SI, reaching the saturation limit of 2.4 % at an axial position of ca. 650 mm, 300 mm beyond the outlet boundary used in all other calculations.

In contrast to the modeling results at 20 slm, our model does predict NO_x saturation with increasing SEI at 6 slm, consistent with the experimental trend. At this lower flow rate, the reduced axial velocity extends the cooling trajectory of the plasma effluent before it reaches the outlet boundary, primarily driven by wall heat losses. As a result, the outlet mixture reaches temperatures where back reactions become negligible, effectively quenching or "freezing" the NO_x concentration. The mechanisms responsible for the observed saturation will be discussed in section 4.3.1.

3.3. Modeling insights on transport and chemistry contributions to NO_x production

3.3.1. Role of convective and diffusive transport in NO_x production

In addition to our model validation, we aim to provide insights into the mechanisms contributing to NO_x production. In each volume element of the simulation domain, the net production or destruction of NO_x due to chemistry should be balanced by transport terms. As such, the total NO_x production can be decomposed into convective and diffusive contributions, which we investigate in this section. In the next section, we will focus on the chemical reactions contributing to the net production or destruction of NO.

Following the approach in [41], we isolate the convective contribution by artificially fixing all molecular and turbulent diffusion coefficients to a very low value, i.e., $D = 10^{-5}$ m^2 s^{-1}. The NO_x production obtained in this way, defined by the molar fraction at the outlet (see equation (16), represents the convective contribution, $x_{NO_x}^{conv}$.

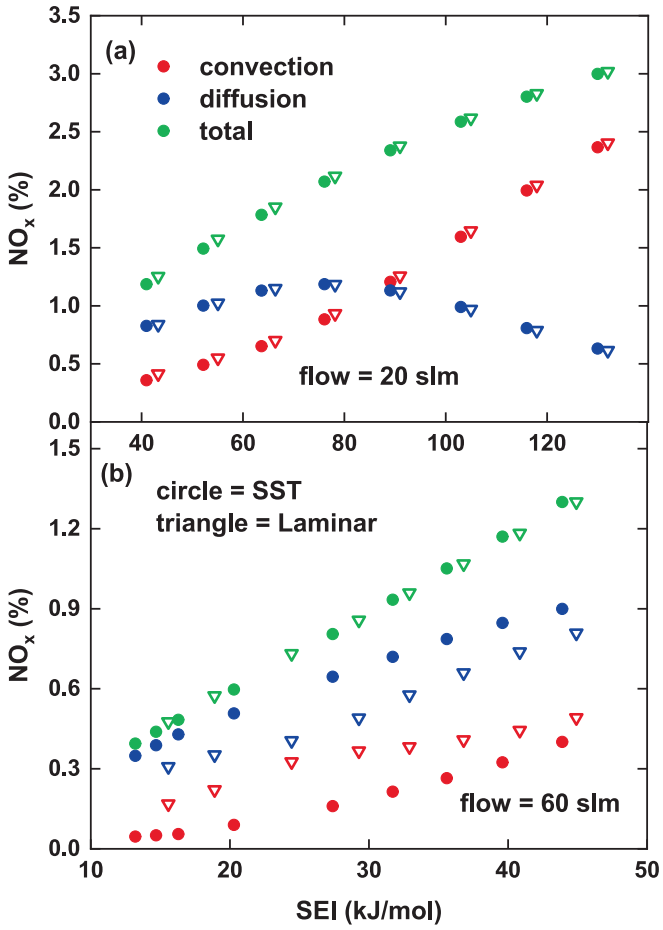

Fig. 10. Contribution of convective and diffusive transport to NO_x production as a function of SEI, for a flow rate of 20 slm (a) and 60 slm (b).

Subsequently, the diffusive contribution is calculated as $x_{NO_x}^{diff} = x_{NO_x} - x_{NO_x}^{conv}$, where x_{NO_x} is the molar fraction obtained from the fully coupled simulation using physical values for the diffusion coefficients.

Fig. 10 plots the NO_x production contributions as a function of SEI, for a flow rate of 20 slm (a) and 60 slm (b). At 20 slm, NO_x production is mainly driven by radial diffusion below SEI values of 80 kJ/mol, although axial convective transport also has a non-negligible contribution. Beyond this threshold, convection becomes the dominant transport mechanism. At 60 slm (Fig. 10 (b)), given that a similar power range was explored, the corresponding SEI values are in a lower range. Due to the limited SEI range covered, the drop in the diffusive contribution to NO_x production with increasing SEI, observed around SEI = 75 kJ/mol for the 20 slm case in Fig. 10 (a), is not seen here, and thus, diffusion has the dominant contribution in the entire SEI range investigated.

As with all conditions studied in this work, both the SST and laminar flow models predict nearly identical NO_x concentrations at the outlet. At 20 slm, both models also agree in their predicted contributions of convective and diffusive transport. In contrast, at 60 slm, a clear difference exists between the convective and diffusive contributions predicted by the SST and laminar models. This indicates that, although the same amount of NO_x is produced at the plasma edge in both cases, the relative importance of quenching mechanisms in the plasma afterglow differs.

Analysis of the modeling results reveals that, in the laminar flow simulations, the NO_x molar flow is transported by a higher axial velocity component (ca. 30 % higher), resulting in a higher convective cooling rate, assuming similar axial temperature gradients. This likely explains the higher NO_x concentration observed in the laminar model when

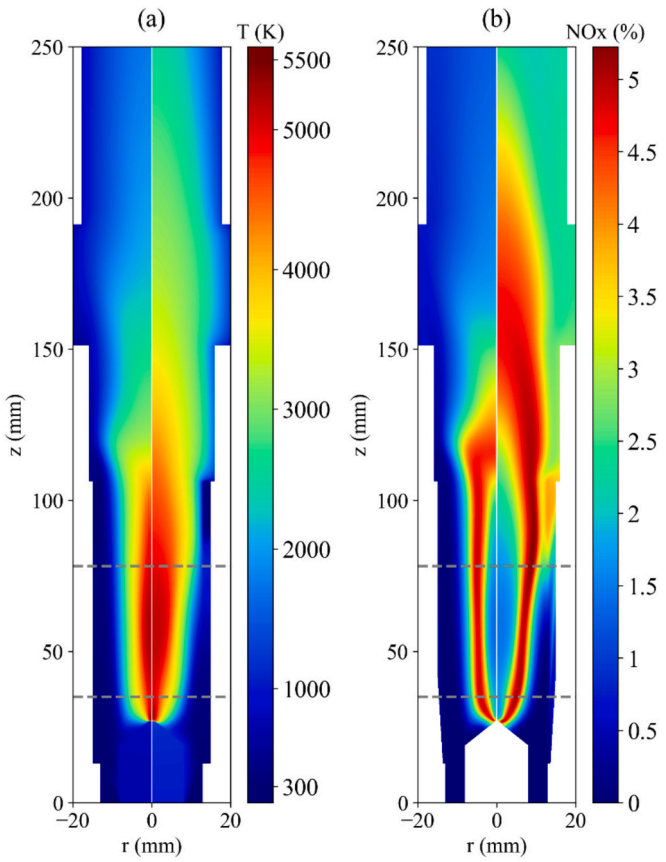

Fig. 11. Temperature (a) and NO_x molar concentration (b) for a flow rate of 20 slm and SEI of 41 kJ/mol (left panels) and flow rate of 6 slm and SEI of 253 kJ/mol (right panels), assuming turbulent (SST) flow.

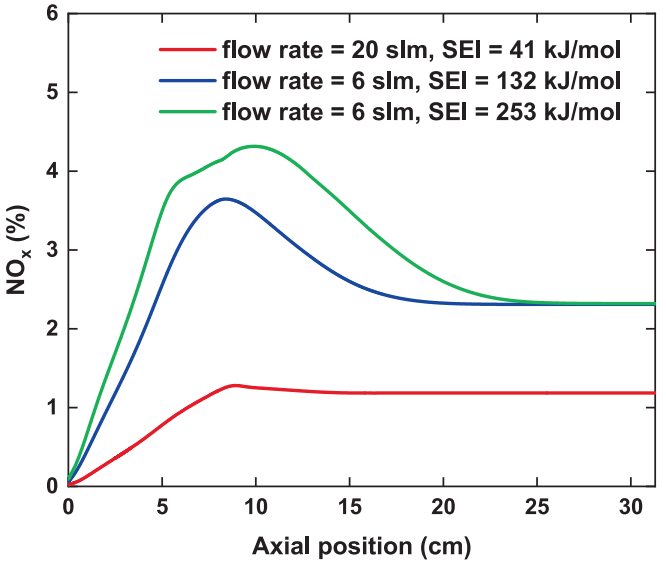

Fig. 12. Radially averaged NO_x concentration as a function of axial position, for a flow rate of 20 slm with SEI = 41 kJ/mol, and a flow rate of 6 slm with SEI = 132 kJ/mol or SEI = 253 kJ/mol, assuming turbulent (SST) flow.

species diffusion is excluded. Although convective quenching is less efficient in the SST model, diffusional quenching, enhanced through the additional turbulent diffusivity compared to laminar flow (effective diffusion coefficient can be a factor 10 higher), is fast enough to effectively quench most of the NO_x present in the plasma effluent in the fully coupled simulations with physical diffusion coefficients, yielding the same total NO_x production for the SST and laminar flow model.

Fig. 11 plots the temperature (a) and NO_x molar concentration (b) profiles, for a flow rate of 20 slm with SEI = 40.3 kJ/mol (left panel) and a flow rate of 6 slm with SEI = 259 kJ/mol (right panel), assuming turbulent (SST) flow. In the lower SEI range (SEI < 80 kJ/mol), the radial gradients in NO_x concentration (cf. figure 11 (b) left panel), as well as gradients in temperature (cf. figure 11 (a) left panel), are sufficiently strong to support a strong radial diffusive flux (in line with Fig. 10), enabling rapid cooling and efficient quenching of the produced NO_x in the cold peripheral gas, as further discussed in section 4.3.2.

Fig. 12 presents the radially averaged NO_x concentration (see equation (16) as a function of axial position in the reactor for a flow rate of 20 slm at SEI = 41 kJ/mol, and for 6 slm at SEI = 132 kJ/mol and SEI = 253 kJ/mol, assuming turbulent (SST) flow. The lowest SEI condition falls within the low-SEI regime discussed earlier. In this case, the NO_x concentration increases up to z = 8.7 cm, corresponding to the region where power deposition by the surface wave significantly decreases, reaching a peak of 1.28 %. Beyond this point, the concentration slightly declines and stabilizes at 1.19 %.

This near-complete quenching of NO_x present in the plasma effluent is attributed to the fact that NO_x contained in the cold peripheral region is minimally affected by back reactions as the temperature remains sufficiently low when travelling downstream. Additionally, NO_x carried in the hotter gas stream that does not diffuse to the cold periphery is also effectively quenched, as heat conduction from the hot to the cold stream ensures a sufficient cooling rate. This mechanism is linked to the convective contribution to NO_x production observed in Fig. 10, as negative temperature gradients along the flow lines enable convective quenching of transported NO_x in the hotter gas stream.

The near-perfect quenching process is linked to the linear increase in NO_x production with rising SEI, as NO_x losses due to back reactions do not scale significantly with SEI, that would otherwise lead to a deviation from the linear increase. In [27], this effective quenching of NO_x in the plasma effluent through mixing with the cold peripheral gas was proposed to explain the observed trends. The present study confirms this interpretation and provides additional insights into the underlying quenching mechanisms.

As shown in Fig. 10, at 20 slm, the diffusive contribution to NO_x production decreases with increasing SEI, while convection becomes the dominant transport mechanism above ca. 85 kJ/mol. This shift corresponds to a change in the quenching mechanism. At higher SEI values, the discharge broadens, flattening radial gradients (cf. Fig. 11, right panels) and reducing the extent of the cold peripheral gas zone responsible for radial diffusive quenching (cf. Fig. 11 (a), right panel). As a result, a larger fraction of the produced NO_x cannot diffuse to the cold periphery and is instead carried downstream by the hot gas flow. At these elevated SEIs, the plasma afterglow cools more slowly due to the reduced extent of the cold peripheral gas zone, which limits conductive heat transfer from the hot core to the periphery. Consequently, convective quenching along the streamlines becomes less effective, leading to increased NO_x losses through back reactions, as evident in Fig. 12 under high-SEI conditions (> 100 kJ/mol).

Consequently, around this threshold of ca. 85 kJ/mol, the linear increase in NO_x concentration with SEI begins to weaken, as the cooling rate provided by axial convective transport is insufficient to efficiently quench the produced NO_x, leading to significant losses through back reactions. Therefore, above SEI values of 80–100 kJ/mol, external cooling should be considered to ensure effective quenching of NO_x.

Fig. 12 provides further insights into the flattening of NO_x production with increasing SEI. Comparing the results at SEI = 253 kJ/mol to those at SEI = 132 kJ/mol, it is evident that more NO_x is generated within the plasma at the highest SEI due to the expanded plasma volume at the optimum temperature (ca. 3100 K [27]). However, this additional NO_x cannot be effectively retained, as the radial temperature gradient and NO_x gradient are too weak, and the cold peripheral gas zone is

insufficient to support radial diffusive quenching near the end of the discharge (cf. Fig. 11 right panels).

Instead, the NO_x concentration decreases as the hot plasma effluent slowly cools down and temperature homogenizes through conductive heat transfer to the reactor walls. Due to weak axial temperature gradients, the NO_x concentration in the hot stream relaxes toward its equilibrium value, as opposed to retaining the higher concentration produced by the plasma. This concentration eventually 'freezes' once the temperature drops below approximately 2100 K, where back reactions become negligible. The final effluent composition at this temperature is nearly identical for SEI > 100 kJ/mol, but is reached further downstream at higher SEIs (cf. Fig. 12) due to the increased thermal load requiring more extensive wall cooling.

Consequently, for SEI > 100 kJ/mol, the additional NO_x produced in the plasma is largely lost during cooling. As a result, without external cooling, our model predicts a maximum outlet NO_x concentration of 2.3 %, which is close to the experimentally observed 2.5 %. Higher NO_x concentrations could be achieved if the effluent were cooled more rapidly (e.g., 10^8 K/s [86]) than through passive wall heat losses, e.g., via nozzles or heat exchangers. The saturation in NO_x production above 100 kJ/mol is not visible in Fig. 10, as the model effluent remains reactive, as previously noted. However, as shown in Sec. 4.2.3, the NO_x concentration still drops when the computational domain is lengthened. This drop follows the same mechanism as described above. We note that when diffusion is artificially suppressed in the extended domain, the convective contribution to NO_x formation decreases, similar to the drop in NO_x concentration for the fully coupled simulation in the extended domain. However, the relative contributions of convection and diffusion to NO_x production remain approximately constant.

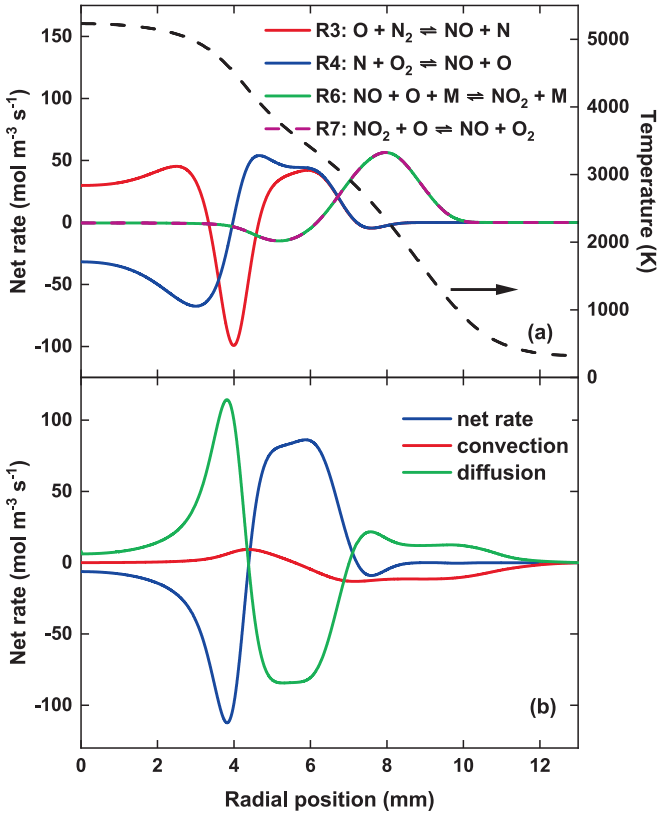

Fig. 13. Net rate of reactions involving NO (left y-axis), i.e., (R3), (R4), (R6) and (R7), and temperature (right y-axis) (a) and net total reactive source term (sum of the rates of all production minus loss reactions) and transport terms of NO (b), as a function of radial position, at the axial position of z = 56 mm, for a flow rate of 20 slm and SEI of 63.7 kJ/mol, assuming turbulent (SST) flow.

3.3.2. *Role of chemical reactions in NO_x production*

To gain further insight into the contributions of chemical reactions to NO_x production, we analyze the radial profiles of the reaction rates involved in the formation and destruction of NO, along with the associated transport terms. Since the reaction pathways differ between NO and NO_2, we do not group them together as NO_x in this analysis, as we did above for the transport terms. Instead, we focus specifically on NO, since NO_2 is formed in negligible quantities, as will be explained in the following paragraphs.

In contrast to the negligible NO_2 concentrations predicted by our model, the measurements of [2] indicate that NO_2 constitutes the dominant fraction of NO_x relative to NO. This discrepancy arises because, in addition to the oxidation of NO by O atoms (R6), which occurs at elevated gas temperatures where significant O atoms are present, NO is also oxidized at lower temperatures via slower pathways [87]. These include the reverse process of R7 and the termolecular reaction $NO + NO + O_2 \rightleftharpoons 2\,NO_2$ [36,87]. Such low-temperature oxidation processes take place downstream in the reactor and connecting tubing, continuing until the gas reaches the detector. Due to computational constraints, our model does not simulate the entire reactor pathway up to the detection point. Therefore, we focus on comparing the total NO_x concentration between model predictions, consisting predominantly of NO, and experimental data, since the slow oxidation of NO only affects the NO/NO_2 ratio without altering the total NO_x yield.

The net rates of reactions involving NO are plotted as a function of radial position in Fig. 13 (a) on the left y-axis, as well as the temperature (right y-axis), at the center of the resonator (z = 56 mm), for the model calculations assuming turbulent (SST) flow. The total reactive source term for NO, i.e., sum of all chemical reactions involving NO, is plotted in Fig. 13 (b), together with the convective and diffusive terms that balance net NO production or destruction. We note that although this reaction rate analysis was conducted solely as a function of radial position along the central cut line of the resonator (z = 56 mm), the underlying mechanisms are representative of the broader reactive domain.

From Fig. 13 (b), it is clear that NO is mainly produced in the radial region between 4.5 mm and 7 mm (characterized by a temperature of 4200 K – 2900 K, cf. Fig. 13 (a)), i.e., the edge of the plasma, where the net rate of both Zeldovich reactions (R3 and R4) is positive. The NO production is mainly balanced by diffusion, as indicated by the diffusive term in Fig. 13 (b), which has similar magnitude but opposite sign. Nearly half of the produced NO (ca. 45 %) diffuses into the hot plasma zone, where it is first mainly destroyed upon the reverse reaction of R3 (cf. Fig. 13 (a), while deeper into the plasma core (closer to the center), the reverse reaction of R4 becomes dominant, as the high temperatures (T > 4300 K) lead to near-complete O_2 dissociation ($x_{O_2} < 1$ %), strongly favoring the reverse process of R4. Additional NO destruction occurs in the hot core region (r < 3 mm) through NO dissociation (R5), although its contribution is minor, i.e., ca. 10 % of the net NO destruction attributed to R4, and is therefore not shown.

R3 shows net production in the hot plasma core, as the high temperatures enable the forward reaction that is usually limited by its high activation barrier associated with the dissociation of N_2. However, it does not compensate for the net negative rate of R4, as seen by the negative reactive source term of NO in Fig. 13 (b) up to r = 0. We note that there is an additional flux of NO to the hot plasma core, driven by radial convective transport resulting from the swirling velocity field. However, this contribution is small compared to the diffusive contribution, as seen in Fig. 13 (b).

As mentioned above, ca. 45 % of the NO produced at the edge of the plasma (4.5 mm < r < 7 mm) is lost due to diffusion into the hot plasma zone, while the remaining fraction diffuses outward toward the periphery. As is clear from Fig. 13 (a), only a small fraction of NO is destroyed via the net reverse Zeldovich reactions (7.2 mm < r < 8.8 mm). The net NO produced across the complete radial cross-section is then transported downstream by axial convection, mainly within the region of 6 mm < r < 12 mm. Axial diffusion has a negligible

contribution due to the weak axial gradients.

As explained in the previous paragraph, radial diffusive transport of NO enables additional NO to be stored in the cooler peripheral gas, resulting in a local NO fraction that exceeds its chemical equilibrium value. Nevertheless, the majority of NO is still transported within the hotter gas region (2000–4000 K, 4.5 mm $< r <$ 8.5 mm), where NO concentrations closely follow equilibrium concentrations. Consequently, the contribution of diffusive transport to the overall NO production within the plasma region remains minor. This is confirmed by a calculation in which we artificially reduce the NO diffusion coefficient to $D = 10^{-5}$ m^2 s^{-1} for axial positions z $<$ 12.5 cm, i.e., the plasma region where the radially averaged NO concentration increases as a function of axial position. This adjustment results in a relatively minor decrease in outlet NO concentration from 1.79 % to 1.42 %. However, diffusive transport remains critical for quenching NO in the effluent, as evidenced by its large contribution to total NO_x production at a flow rate of 20 slm and SEI of 60 kJ/mol, as shown in Fig. 10.

Fig. 13 (a) demonstrates that the net rate of NO oxidation (R6) closely matches the rate of NO_2 destruction by O atoms (R7) across the entire reactor cross section. Because the NO consumed via R6 is immediately regenerated through R7, this sequence does not alter the overall NO concentration in the system. Instead, the combined action of R6 and R7 forms an effective catalytic cycle for O atom recombination.

In the region 3.5 mm $< r <$ 6.2 mm, corresponding to temperatures between 3300 K and 4800 K, R6 and R7 exhibit slightly negative net rates, contributing slightly to O_2 dissociation. However, this contribution is minor compared to the direct dissociation via R2 (see Fig. S.9 in the SI). In contrast, for 6.2 mm $< r <$ 10 mm (900 K – 3300 K), the net positive rates of R6 and R7 significantly enhance O atom recombination, becoming the dominant recombination pathway beyond r $>$ 7.2 mm (cf. Fig. S.9).

As shown in Fig. 13 (a), the R6–R7 cycle operates in temperature regions where the reverse process of R3 contributes to NO destruction (r $<$ 8.8 mm). By removing O atoms, this cycle increases the net rate of R3, thereby enhancing overall NO_x production. For example, at a flow rate of 6 slm and SEI = 132 kJ/mol, excluding R7 reduces the total NO_x concentration from 2.31 % to 1.97 %. Thus, the inclusion of R6 and R7 is essential for accurately capturing NO_x formation dynamics, particularly at higher SEI values where reverse reactions play a crucial role.

In [20], it was hypothesized that NO oxidation via R6 enhances NO_x yield by converting NO into NO_2, thereby shielding it from back reactions. Our modeling results suggest this is only partially correct. While NO oxidation does enhance NO_x formation, it does so, not by stabilizing NO as inert NO_2, but through the catalytic cycle formed by R6 and R7. This cycle removes O atoms that would otherwise participate in NO destruction via the reverse Zeldovich mechanism, thereby promoting net NO_x formation.

As mentioned in the Introduction, our group has experimentally demonstrated that NO_x production in RGA plasma operating in air at elevated pressure (up to 3 barg) yields significant improvements, especially in terms of higher NO_x production rates, at record-low EC of 1.8 MJ/mol [20]. Our novel modeling insights now suggest an additional advantage of operating at higher pressures, besides the increased NO_x equilibrium concentrations achievable under such conditions [20]. Specifically, the increased gas density at higher pressures enhances the three-body reaction rate of NO oxidation (R6), thereby promoting O atom recombination and reducing NO destruction via O atoms (R3).

Hence, based on our modeling insights, we recommend operating at elevated pressures to enhance the equilibrium fraction of NO_x and suppress back reactions by accelerating NO oxidation that effectively removes O atoms from regions where they would otherwise contribute to NO destruction. Furthermore, since NO_x formation in chemical equilibrium is most efficient at ca. 3100 K (2.7 MJ/mol), the system performance can be optimized by achieving a uniform mixture temperature near this value. However, the SEIs required to heat and dissociate air to an equilibrium mixture at 3100 K already approach 120 kJ/mol, as calculated via thermodynamic equilibrium calculations using the NASA 9 polynomials [70] in CANTERA [71]. Our analysis indicates that convective quenching resulting from passive wall cooling is not fast enough at these higher SEIs above 80 kJ/mol. As a result, significant NO_x losses occur due to back reactions. Therefore, the uniform mixture at the optimal temperature should be rapidly quenched (by means of quenching nozzles or other strategies) to temperatures below ca. 2100 K, where reverse Zeldovich reactions are effectively frozen. Below this temperature threshold of ca. 2100 K, the mixture can be cooled more gradually, allowing recovery of the effluent heat to preheat the inlet air stream, so that less power is needed to reach the same NO_x production, thereby further reducing the overall EC of NO_x formation.

4. Conclusions and perspective

We have developed a fluid model for (near-)atmospheric pressure air MW plasma that resolves MW field heating by solving the wave equation and incorporates turbulent flow effects. Since our new model does not rely on predefined field variables obtained from experiments, it holds potential to independently predict experimental outcomes.

We have validated our model against the experiments of [1] (SEI $<$ 52 kJ/mol), where the assumption of laminar flow yields good agreement with the measured temperature profile. The SST turbulence model predicts a more contracted plasma due to enhanced radial conductive heat losses. Both the SST and laminar flow models accurately reproduce the outlet NO_x concentrations, indicating that turbulence has a limited effect on NO_x formation.

Next, we validated our model against the experiments of [2], which span a broader range of flow rates (5–90 slm) and SEI values (10–300 kJ/mol). Reasonable agreement was observed for the electron density at the plasma core, suggesting a reliable prediction of the maximum plasma temperature as well. Both the SST and laminar flow models accurately reproduce the experimental NO_x concentrations across the complete SEI range.

After the model validation, we investigated the mechanisms contributing to NO_x production, considering both chemistry and transport effects. Our results indicate that radial diffusive transport dominates NO_x formation for SEI values below 85 kJ/mol. As SEI increases, the cold peripheral gas zone that enables radial diffusive quenching decreases, and convective transport becomes the primary contributor to NO_x production above this threshold. Around the same SEI value, external cooling becomes necessary to prevent significant NO_x losses through back reactions. Reaction rate analysis reveals that NO is primarily formed at the plasma edge, with approximately half of it diffusing inward and being destroyed, while the other half diffuses outward, where it is transported downstream via axial convection.

Our modeling results also indicate an additional advantages of operating at elevated pressures, besides the enhanced equilibrium concentrations of NO_x achievable under such conditions. Specifically, higher pressure enhances NO oxidation rates, which, together with NO_2 destruction by O atoms, forms a catalytic cycle for O atom recombination. This cycle effectively removes O atoms from regions where they would otherwise contribute to NO destruction, thereby increasing NO_x production.

In addition to operating at elevated pressures (e.g., $>$10 bar), thermal plasma-based NO_x formation from air can be optimized by maintaining a uniform mixture temperature of ca. 3100 K for efficient NO_x production (2.7 MJ/mol), thereby avoiding a hot plasma core with excessively high temperatures where NO_x is mainly destroyed. This should be followed by rapid quenching to below ca. 2100 K to freeze the reverse Zeldovich reactions. Below this temperature, the effluent can be cooled more gradually, allowing heat recovery to preheat the inlet air stream and reduce the overall EC of NO_x production.

Overall, our new model reliably predicts NO_x production without requiring experimental input for parameter fitting. Our next step will be to utilize this predictive capability in the design of plasma reactor

configurations, possibly operating at higher pressure, that optimize post-plasma quenching and heat recovery, with the goal of significantly reducing the EC of thermal MW plasma-based NO_x production from air, aiming to reach the EC target of 1–1.5 MJ/mol defined by Rouwenhorst et al. for the plasma process to become competitive with the HB-Ostwald process [26].

CRediT authorship contribution statement

Matthias Albrechts: Writing – original draft, Validation, Methodology, Investigation, Conceptualization. **Ivan Tsonev:** Writing – review & editing, Supervision, Methodology, Investigation, Conceptualization. **Vojtěch Laitl:** Writing – review & editing, Methodology, Investigation, Conceptualization. **Annemie Bogaerts:** Writing – review & editing, Supervision, Resources, Project administration, Funding acquisition, Conceptualization.

Declaration of competing interest

The authors declare that they have no known competing financial interests or personal relationships that could have appeared to influence the work reported in this paper.

Acknowledgements

We thank Dr. Mariagrazia Troia for sharing detailed information about the experimental setup of [2] and for the insightful discussions regarding the interpretation of our modeling results. This research was supported by the Horizon Europe Framework Program “Research and Innovation Actions” (RIA), project CANMILK (Grant No. 101069491), the FWO postdoc project of I. Tsonev (grant ID 1220326 N), the European Research Council (ERC) under the European Union’s Horizon 2020 research and innovation programme (grant agreement No. 810182–SCOPE ERC Synergy project) and the Excellence of Science FWO-FNRS project (FWO grant ID G0I1822N; EOS ID 40007511).

Appendix A. Supplementary data

Supplementary data to this article can be found online at https://doi.org/10.1016/j.enconman.2025.120842.

Data availability

No data was used for the research described in the article.

References

[1] Tatar M, Vashisth V, Iqbal M, Butterworth T, van Rooij G, Andersson R. Analysis of a plasma reactor performance for direct nitrogen fixation by use of three-dimensional simulations and experiments. Chem Eng J 2024;497:154756.
[2] Troia M, Vagkidis C, Schulz A, Köhn-Seemann A, Walker M, Tovar GE. NOx Production via an Atmospheric Microwave Air Plasma Torch. Chem Ing Tech 2025;97(5):435–43.
[3] Tanabe Y, Nishibayashi Y. Developing more sustainable processes for ammonia synthesis. Coord Chem Rev 2013;257(17–18):2551–64.
[4] Brightling J. Ammonia and the fertiliser industry: the development of ammonia at Billingham. Johnson Matthey Technol Rev 2018;62(1):32–47.
[5] Rouwenhorst KH, Jardali F, Bogaerts A, Lefferts L. From the Birkeland–Eyde process towards energy-efficient plasma-based NO X synthesis: a techno-economic analysis. Energ Environ Sci 2021;14(5):2520–34.
[6] Bogaerts A, Neyts EC. Plasma technology: an emerging technology for energy storage. ACS Energy Lett 2018;3(4):1013–27.
[7] Bogaerts A. Plasma technology for the electrification of chemical reactions. Nat Chem Eng 2025:1–5.
[8] Li S, Medrano JA, Hessel V, Gallucci F. Recent progress of plasma-assisted nitrogen fixation research: a review. Processes 2018;6(12):248.
[9] Rusanov VD, Fridman A, Sholin GVE. The physics of a chemically active plasma withnonequilibrium vibrational excitation of molecules. *soviet*. Physics Uspekhi 1981;24(6):447.
[10] Bahnamiri OS, Verheyen C, Snyders R, Bogaerts A, Britun N. Nitrogen fixation in pulsed microwave discharge studied by infrared absorption combined with modelling. Plasma Sources Sci Technol 2021;30(6):065007.
[11] Klimek A, Piercey DG. Nitrogen fixation via plasma-assisted processes: mechanisms, applications, and comparative analysis—a comprehensive review. Processes 2024;12(4):786.
[12] Chen H, Yuan D, Wu A, Lin X, Li X. Review of low-temperature plasma nitrogen fixation technology. Waste Disposal Sustainable Energy 2021;3:201–17.
[13] Mutel B, Dessaux O, Goudmand P. Energy cost improvement of the nitrogen oxides synthesis in a low pressure plasma. Revue de physique appliquée 1984;19(6):461–4.
[14] Asisov R, Givotov V, Rusanov V, Fridman A. High energy chemistry (Khimia Vysokikh energij). Sov Phys 1980;14:366.
[15] Vervloessem E, Aghaei M, Jardali F, Hafezkhiabani N, Bogaerts A. Plasma-based n2 fixation into no x: insights from modeling toward optimum yields and energy costs in a gliding arc plasmatron. ACS Sustain Chem Eng 2020;8(26):9711–20.
[16] Li Y, Luo Y, Man C, Pei X, Lu X, Graves DB. Enhancing nitrogen fixation efficiency in glow-like discharge by reducing cathode-fall voltage. Plasma Sources Sci Technol 2024;33(10):105014.
[17] Pei X, Li Y, Luo Y, Man C, Zhang Y, Lu X, et al. Nitrogen fixation as NOx using air plasma coupled with heterogeneous catalysis at atmospheric pressure. Plasma Processes Polym 2024;21(1):2300135.
[18] Jardali F, Van Alphen S, Creel J, Eshtehardi HA, Axelsson M, Ingels R, et al. NO x production in a rotating gliding arc plasma: potential avenue for sustainable nitrogen fixation. Green Chem 2021;23(4):1748–57.
[19] Van Alphen S, Eshtehardi HA, O’Modhrain C, Bogaerts J, Van Poyer H, Creel J, et al. Effusion nozzle for energy-efficient NOx production in a rotating gliding arc plasma reactor. Chem Eng J 2022;443:136529.
[20] Tsonev I, O’Modhrain C, Bogaerts A, Gorbanev Y. Nitrogen fixation by an arc plasma at elevated pressure to increase the energy efficiency and production rate of no x. ACS Sustain Chem Eng 2023;11(5):1888–97.
[21] Abdelaziz AA, Teramoto Y, Nozaki T, Kim H-H. Performance of high-frequency spark discharge for efficient NOx production with tunable selectivity. Chem Eng J 2023;470:144182.
[22] Zamri AA, Ong MY, Nomanbhay S, Show PL. Microwave plasma technology for sustainable energy production and the electromagnetic interaction within the plasma system: a review. Environ Res 2021;197:111204.
[23] Tiwari S, Caiola A, Bai X, Lalsare A, Hu J. Microwave plasma-enhanced and microwave heated chemical reactions. Plasma Chem Plasma Process 2020;40(1):1–23.
[24] Füner M, Wild C, Koidl P. Simulation and development of optimized microwave plasma reactors for diamond deposition. Surf Coat Technol 1999;116:853–62.
[25] Kelly S, Bogaerts A. Nitrogen fixation in an electrode-free microwave plasma. Joule 2021;5(11):3006–30.
[26] Rouwenhorst KH, Jardali F, Bogaerts A, Lefferts L. Correction: from the Birkeland–Eyde process towards energy-efficient plasma-based NO X synthesis: a techno-economic analysis. Energ Environ Sci 2023;16(12):6170–3.
[27] Tsonev I, Eshtehardi HA, Delplancke M-P, Bogaerts A. Importance of geometric effects in scaling up energy-efficient plasma-based nitrogen fixation. Sustainable Energy Fuels 2024;8(10):2191–209.
[28] Hurlbatt A, Gibson AR, Schröter S, Bredin J, Foote APS, Grondein P, et al. Concepts, capabilities, and limitations of global models: a review. Plasma Processes Polym 2017;14(1–2):1600138.
[29] Albrechts M, Tsonev I, Bogaerts A. Investigation of O atom kinetics in O2 plasma and its afterglow. Plasma Sources Sci Technol 2024;33(4):045017.
[30] Cejas E, Mancinelli BR, Prevosto L. Glow discharge in a high-velocity air flow: the role of the associative ionization reactions involving excited atoms. Materials 2019;12(16):2524.
[31] Minesi NQ, Mariotto PB, Pannier E, Vincent-Randonnier A, Stancu GD, Laux CO. Kinetic mechanism and sub-ns measurements of the thermal spark in air. Plasma Sources Sci Technol 2023;32(4):044005.
[32] Silva T, Bera S, Pintassilgo CD, Herrmann A, Welzel S, Tsampas MN, et al. Unraveling NO production in N2–O2 plasmas with 0D kinetic modeling and experimental validation. Chem A Eur J 2024;128(34):7235–56.
[33] Fox RO. CFD models for analysis and design of chemical reactors. Adv Chem Eng 2006;31:231–305.
[34] Naidis G. Simulation of convection-stabilized low-current glow and arc discharges in atmospheric-pressure air. Plasma Sources Sci Technol 2007;16(2):297.
[35] Babaeva NY, Naidis G. Simulation of low-current DC discharges in longitudinal flows of atmospheric-pressure air. Plasma Sources Sci Technol 2024;33(5):055013.
[36] Wnukowski, M.; Modliński, N.; Amasi, U. L., Unveiling the Impact of a Nozzle on Nox Formation in Atmospheric Microwave Plasma. *Available at SSRN 5334026*.
[37] Majeed M, Iqbal M, Altin M, Kim Y-N, Dinh DK, Lee C, et al. Effect of thermal gas quenching on NOx production by atmospheric pressure rotating arc Plasma: a pathway towards Eco-Friendly fertilizer. Chem Eng J 2024;485:149727.
[38] Van Alphen S, Jardali F, Creel J, Trenchev G, Snyders R, Bogaerts A. Sustainable gas conversion by gliding arc plasmas: a new modelling approach for reactor design improvement. Sustainable Energy Fuels 2021;5(6):1786–800.
[39] Marnef RQ, Maerivoet S, Tsonev I, Reniers F, Bogaerts A. Spatially resolved modelling of NH3 cracking in warm plasma. Chem Eng J 2025;161180.
[40] Maerivoet S, Tsonev I, Slaets J, Reniers F, Bogaerts A. Coupled multi-dimensional modelling of warm plasmas: Application and validation for an atmospheric pressure glow discharge in CO2/CH4/O2. Chem Eng J 2024;492:152006.
[41] Van Poyer HM, Tsonev I, Maerivoet SJ, Albrechts MC, Bogaerts A. Influence of radial transport and turbulent effects on CO2 conversion in a microwave plasma reactor: Insights from a multi-dimensional thermo-chemical flow model. Chem Eng J 2025;507:160688.

[42] Jimenez-Diaz M, Carbone E, van Dijk J, Van der Mullen J. A two-dimensional Plasimo multiphysics model for the plasma–electromagnetic interaction in surface wave discharges: the surfatron source. J Phys D Appl Phys 2012;45(33):335204.
[43] Georgieva V, Berthelot A, Silva T, Kolev S, Graef W, Britun N, et al. Understanding microwave surface-wave sustained plasmas at intermediate pressure by 2D modeling and experiments. Plasma Processes Polym 2017;14(4–5):1600185.
[44] Tatarova E, Dias F, Felizardo E, Henriques J, Pinheiro M, Ferreira C, et al. Microwave air plasma source at atmospheric pressure: Experiment and theory. J Appl Phys 2010;108(12).
[45] Baeva M, Hempel F, Baierl H, Trautvetter T, Foest R, Loffhagen D. Two-and three-dimensional simulation analysis of microwave excited plasma for deposition applications: operation with argon at atmospheric pressure. J Phys D Appl Phys 2018;51(38):385202.
[46] Kabouzi Y, Graves D, Castaños-Martínez E, Moisan M. Modeling of atmospheric-pressure plasma columns sustained by surface waves. Physical review E—statistical, nonlinear, and soft matter. Physics 2007;75(1):016402.
[47] Baeva, M.; Rackow, K.; Becker, M.; Ehlbeck, J.; Loffhagen, D., Characterization of atmospheric pressure microwave plasma in N2/O2/H2O gas mixtures. *Topic C9, 30th ICPIG, Belfast, Northern Ireland UK* **2011**.
[48] Laitl V, Tsonev I, Biondo O, Carbone E, Albrechts MC, Bogaerts A. Fluid–electromagnetic modelling of atmospheric pressure CO_2 microwave plasma: Towards reactor design. Chemical Engineering Journal 2025:171039.
[49] Hecimovic A, Kiefer C, Meindl A, Antunes R, Fantz U. Fast gas quenching of microwave plasma effluent for enhanced CO2 conversion. J CO2 Util 2023;71:102473.
[50] *COMSOL Multiphysics® v. 6.0. www.comsol.com. COMSOL AB, Stockholm, Sweden.*.
[51] Troia, M., private communication.
[52] Menter FR, Kuntz M, Langtry R. Ten years of industrial experience with the SST turbulence model. Turbulence, heat and mass transfer 2003;4(1):625–32.
[53] Roldughin, V., The Chapman-Enskog theory and non-equilibrium thermodynamics. **1984**.
[54] Kays WM. Turbulent Prandtl number where are we? ASME J Heat Trans 1994;116(2):284–95.
[55] Baulch D, Bowman CT, Cobos CJ, Cox RA, Just T, Kerr J, et al. Evaluated kinetic data for combustion modeling: supplement II. J Phys Chem Ref Data 2005;34(3):757–1397.
[56] Aleksandrov N, Bazelyan E, Kochetov I, Dyatko N. The ionization kinetics and electric field in the leader channel in long air gaps. J Phys D Appl Phys 1997;30(11):1616.
[57] Tsang, W.; Herron, J. T., Chemical kinetic data base for propellant combustion I. Reactions involving NO, NO2, HNO, HNO2, HCN and N2O. *Journal of physical and chemical reference data* **1991**, *20* (4), 609-663.
[58] Atkinson R, Baulch DL, Cox RA, Crowley JN, Hampson RF, Hynes RG, et al. Evaluated kinetic and photochemical data for atmospheric chemistry: volume I-gas phase reactions of O x, HO x, NO x and SO x species. Atmos Chem Phys 2004;4(6):1461–738.
[59] Vass M, Schulenberg D, Donkó Z, Korolov I, Hartmann P, Schulze J, et al. A new 2D fluid-MC hybrid approach for simulating nonequilibrium atmospheric pressure plasmas: density distribution of atomic oxygen in radio-frequency plasma jets in He/O2 mixtures. Plasma Sources Sci Technol 2024;33(1):015012.
[60] Liu Y, Korolov I, Hemke T, Bischoff L, Hübner G, Schulze J, et al. Electron heating mode transitions in radio-frequency driven micro atmospheric pressure plasma jets in He/O2: a fluid dynamics approach. J Phys D Appl Phys 2021;54(27):275204.
[61] Lieberman MA, Lichtenberg AJ. Principles of plasma discharges and materials processing. MRS Bull 1994;30(12):899–901.
[62] Bergman TL, Lavine AS, Incropera FP, DeWitt DP. *Introduction to heat transfer*. John Wiley & Sons; 2011.
[63] Seemann HE. The thermal and electrical conductivity of fused quartz as a function of temperature. Phys Rev 1928;31(1):119.
[64] Moisan M, Zakrzewski Z. Plasma sources based on the propagation of electromagnetic surface waves. J Phys D Appl Phys 1991;24(7):1025.
[65] Zhang W, Yang Y, Peng R, Han D, Wu L, Tao J, et al. Validity of 2-D axisymmetric simplification in modeling microwave discharges in waveguide-based plasma sources. IEEE Trans Plasma Sci 2024.
[66] Hagelaar G, Makasheva K, Garrigues L, Boeuf J-P. Modelling of a dipolar microwave plasma sustained by electron cyclotron resonance. J Phys D Appl Phys 2009;42(19):194019.
[67] Marnef RQ, Maerivoet S, Tsonev I, Reniers F, Bogaerts A. Spatially resolved modelling of NH3 cracking in warm plasma. Chem Eng J 2025;508:161180.
[68] Cejas E, Mancinelli B, Prevosto L. Modelling of an atmospheric–pressure air glow discharge operating in high–gas temperature regimes: the role of the associative ionization reactions involving excited atoms. Plasma 2020;3(1):12–26.
[69] Vialetto L, van de Steeg A, Viegas P, Longo S, Van Rooij GJ, van de Sanden M, et al. Charged particle kinetics and gas heating in CO2 microwave plasma contraction: comparisons of simulations and experiments. Plasma Sources Sci Technol 2022;31(5):055005.
[70] McBride BJ. *NASA Glenn coefficients for calculating thermodynamic properties of individual species*. National Aeronautics and Space Administration. John H Glenn Research Center … 2002.
[71] Goodwin DG, Moffat HK, Cantera RS. An object-oriented software toolkit for chemical kinetics, thermodynamics, and transport processes. Pasadena: Caltech; 2009.
[72] IST-Lisbon database, www.lxcat.net, retrieved on April 10, 2025.
[73] Morgan database, www.lxcat.net, retrieved on April 10, 2025.
[74] Phelps database, www.lxcat.net, retrieved on April 10, 2025.
[75] Shigeta M. Turbulence modelling of thermal plasma flows. J Phys D Appl Phys 2016;49(49):493001.
[76] Tsonev I, Boothroyd J, Kolev S, Bogaerts A. Simulation of glow and arc discharges in nitrogen: effects of the cathode emission mechanisms. Plasma Sources Sci Technol 2023;32(5):054002.
[77] Kabouzi Y, Calzada M, Moisan M, Tran K, Trassy C. Radial contraction of microwave-sustained plasma columns at atmospheric pressure. J Appl Phys 2002;91(3):1008–19.
[78] Kotov V, Kiefer C, Hecimovic A. Validation of the thermo-chemical approach to modelling of CO2 conversion in sub-atmospheric pressure microwave gas discharges. Plasma Sources Sci Technol 2024;33(6):065012.
[79] Leins M, Baumgärtner KM, Walker M, Schulz A, Schumacher U, Stroth U. Studies on a Microwave-Heated Atmospheric Plasma Torch. Plasma Processes Polym 2007;4(S1):S493–7.
[80] Moisan M, Nowakowska H. Contribution of surface-wave (SW) sustained plasma columns to the modeling of RF and microwave discharges with new insight into some of their features. a survey of other types of SW discharges. Plasma Sources Sci Technol 2018;27(7):073001.
[81] Shamami K, Birouk M. Assessment of the performances of RANS models for simulating swirling flows in a can-combustor. Open Aerospace Eng J 2008;1:8–27.
[82] Balabel A, Hegab A, Nasr M, El-Behery SM. Assessment of turbulence modeling for gas flow in two-dimensional convergent–divergent rocket nozzle. App Math Model 2011;35(7):3408–22.
[83] Kim G, Kang W, Bak MS. On the necessary condition for the generation of atmospheric-pressure electrodeless microwave plasma. J Phys D Appl Phys 2025.
[84] Sun H, Lee J, Im S-K, Bak MS. Optical emission spectroscopic studies on atmospheric electrodeless microwave plasma in carbon dioxide–hydrogen mixture. IEEE Trans Plasma Sci 2017;45(12):3154–9.
[85] D'Isa F, Carbone E, Hecimovic A, Fantz U. Performance analysis of a 2.45 GHz microwave plasma torch for CO2 decomposition in gas swirl configuration. Plasma Sources Sci Technol 2020;29(10):105009.
[86] Shen Q, Aleksandr P, Peeters F, Guerra V, Van de Sanden R. Pinpointing energy transfer mechanisms in the quenching process of microwave air plasma. J Phys D Appl Phys 2025.
[87] Patil BS, Peeters F, van Rooij GJ, Medrano J, Gallucci F, Lang J, et al. Plasma assisted nitrogen oxide production from air: using pulsed powered gliding arc reactor for a containerized plant. AIChE J 2018;64(2):526–37.